



## RESEARCH ARTICLE

10.1002/2015JD024722

## Key Points:

- UDTcDA with prior surface reflectance database support is proposed
- UDTcDA detects clouds more effectively than current MODIS cloud mask products
- UDTcDA can be applied to different satellite data and achieve large-scale and long-term cloud detection

## Correspondence to:

J. Wei,  
weijing\_rs@163.com

## Citation:

Sun, L., et al. (2016), A Universal Dynamic Threshold Cloud Detection Algorithm (UDTCDA) supported by a prior surface reflectance database, *J. Geophys. Res. Atmos.*, 121, 7172–7196, doi:10.1002/2015JD024722.

Received 28 DEC 2015

Accepted 3 JUN 2016

Accepted article online 6 JUN 2016

Published online 24 JUN 2016

## A Universal Dynamic Threshold Cloud Detection Algorithm (UDTCDA) supported by a prior surface reflectance database

**Lin Sun<sup>1</sup>, Jing Wei<sup>1</sup>, Jian Wang<sup>2</sup>, Xuetong Mi<sup>1</sup>, Yamin Guo<sup>2</sup>, Yang Lv<sup>3</sup>, Yikun Yang<sup>1</sup>, Ping Gan<sup>1</sup>, Xueying Zhou<sup>1</sup>, Chen Jia<sup>1</sup>, and Xinpeng Tian<sup>1</sup>**

<sup>1</sup>Geomatics College, Shandong University of Science and Technology, Qingdao, China, <sup>2</sup>School of Geography, Beijing Normal University, Beijing, China, <sup>3</sup>State Environmental Protection Key Laboratory of Satellite Remote Sensing, Institute of Remote Sensing and Digital Earth, Chinese Academy of Sciences, Beijing, China

**Abstract** Conventional cloud detection methods are easily affected by mixed pixels, complex surface structures, and atmospheric factors, resulting in poor cloud detection results. To minimize these problems, a new Universal Dynamic Threshold Cloud Detection Algorithm (UDTCDA) supported by a priori surface reflectance database is proposed in this paper. A monthly surface reflectance database is constructed using long-time-sequenced MODerate resolution Imaging Spectroradiometer surface reflectance product (MOD09A1) to provide the surface reflectance of the underlying surfaces. The relationships between the apparent reflectance changes and the surface reflectance are simulated under different observation and atmospheric conditions with the 6S (Second Simulation of the Satellite Signal in the Solar Spectrum) model, and the dynamic threshold cloud detection models are developed. Two typical remote sensing data with important application significance and different sensor parameters, MODIS and Landsat 8, are selected for cloud detection experiments. The results were validated against the visual interpretation of clouds and Cloud-Aerosol Lidar and Infrared Pathfinder Satellite Observation cloud measurements. The results showed that the UDTcDA can obtain a high precision in cloud detection, correctly identifying cloudy pixels and clear-sky pixels at rates greater than 80% with error rate and missing rate of less than 20%. The UDTcDA cloud product overall shows less estimation uncertainty than the current MODIS cloud mask products. Moreover, the UDTcDA can effectively reduce the effects of atmospheric factors and mixed pixels and can be applied to different satellite sensors to realize long-term, large-scale cloud detection operations.

### 1. Introduction

Clouds pose a difficult challenge in the extraction of atmospheric or surface information using remote sensing satellite data [Greenhough et al., 2005; Nakajima et al., 2011]. Clouds affect the radiation energy transmission between land objects and the satellite sensors, seriously decreasing the retrieval accuracy of atmospheric or surface parameters [Li et al., 2011; Kazantzidis et al., 2011, 2013]. In addition, the multiple types of clouds and the complexity of land structures hinder the detection of clouds using remote sensing images with high precision [Jedlovec et al., 2008; Hagolle et al., 2010].

Currently, the threshold method, statistical method, artificial neural network method, and object-oriented method are four primary methods that have been widely used for different satellite sensors. The threshold method uses the difference between clear and cloudy pixels to detect clouds, and several cloud detection algorithms have been developed and applied to various projects based on it, such as the ISCCP (International Satellite Cloud Climatology Project) cloud mask algorithm, the APOLLO (AVHRR Processing scheme Over cLOUDs, Land, and Ocean) cloud mask algorithm, the CLAVR (Clouds from the Advanced Very high Resolution Radiometer) cloud mask algorithm, the CO<sub>2</sub> slicing cloud mask algorithm, and the MODIS (MODerate resolution Imaging Spectroradiometer) cloud mask algorithm.

The ISCCP cloud mask algorithm utilizes the visible narrow band (0.6 μm) and infrared window (11 μm) channels. A pixel is classified as cloudy only if at least one radiance value is distinct from the inferred clear value by an amount larger than the uncertainty in that clear threshold value. The uncertainty can be caused both by measurement errors and by natural variability. The algorithm is constructed to be cloud conservative, minimizing false cloud detections but missing clouds that resemble clear conditions [Rossow and Schiffer, 1991; Sèze and Rossow, 1991; Rossow and Garder, 1993]. The APOLLO cloud mask algorithm uses the first

©2016. The Authors.

This is an open access article under the terms of the Creative Commons Attribution-NonCommercial-NoDerivs License, which permits use and distribution in any medium, provided the original work is properly cited, the use is non-commercial and no modifications or adaptations are made.

through the fifth AVHRR channels at full spatial resolution and is based on five threshold tests. A pixel is defined as clear if all spectral measures fall on the “clear-sky” sides of the various thresholds or is defined as cloud contaminated if the pixel fails any single test; thus, this algorithm is clear-sky conservative [Saunders and Kriebel, 1988; Kriebel et al., 2003]. The CLAVR cloud mask algorithm uses a series of spectral and spatial variability tests to detect clouds with the Cloud and Surface Parameter Retrieval, focusing on the polar areas. The CLAVR algorithm characterizes the variability of scenes, utilizing the fact that uniform scenes are less likely to contain partial or subpixel clouds that other tests fail to detect [Stowe et al., 1991; Liu and Wu, 2004]. CO<sub>2</sub> slicing has been used to distinguish transmissive clouds from opaque clouds and clear sky using infrared radiances in the carbon dioxide-sensitive portion of the spectrum [Wylie and Menzel, 1989; Wylie et al., 1994; Hutchinson and Hardy, 1995; Turner et al., 2001; Gao et al., 2003]. The MODIS cloud mask algorithm benefits from an extended spectral coverage coupled with high spatial resolution and radiometric accuracy. In this algorithm, an established effective method has been adapted to create a high-quality cloud mask project for the global data obtained from MODIS and mitigate some difficulties experienced by previous algorithms, such as thin cirrus, fog and low-level stratus at night, and small-scale cumulus, which are difficult to detect because of insufficient contrast with the surface radiance. This algorithm uses 22 of the 36 channels from visible to thermal infrared ranges to detect cloudy pixels [Ackerman et al., 2010].

The statistical methods detect clouds with regression equations established utilizing statistics and analysis of the difference in the apparent reflectance or brightness temperature among the clear and cloudy pixels in the satellite data. This method can effectively detect clouds in specific data. However, this method is not widely used because the sample data used for the regression model are historical; thus, the application is limited to a specific time and area [Molnar and Coakley, 1985; Kärner, 2000]. The artificial neural network methods attempt to identify the proper network weights and best thresholds from training samples to achieve cloud detection. This method can achieve automatic cloud detection and great accuracy with self-organizing and self-adapting capabilities. However, because the principle of such a method is unclear, training and validation samples are required to cover most conditions of land surface and cloud type. Because the conditions are not specified during training, this method is less accurate [Karlsson, 1989; Clark and Boyce, 1999; Walder and Maclarens, 2000]. The object-oriented method is designed to segment the images into meaningful “objects,” which can be described as a set of features, and realizes the “object” classification by the established relations or differences between the object and class structure. This method can achieve multiscale image segmentation and achieve a high level of cloud detection by making full use of related features, including color, shape, texture and level, and multiscale information. However, the object-oriented method is more appropriate for feature extraction of high-resolution images with rich texture features and is slow in feature selection, possibly missing the optimal eigenvalues [Zhu and Woodcock, 2012; Fisher, 2014; Zhang et al., 2014; Zhu et al., 2015].

The threshold method is the most popular method used for cloud detection because of its high accuracy and stable results. These algorithms aim to obtain a series of proper thresholds of apparent reflectance or brightness temperatures via certain channels for different sensors and achieve cloud detection with reliable accuracy. However, for complex land surface composition and cloud types, it is difficult to identify proper thresholds from any wavelength to accurately detect a cloud. In fact, the threshold to separate the clear pixel from the cloudy is closely related to surface features. Thus, this paper proposes a Universal Dynamic Threshold Cloud Detection Algorithm (UDTCDA) supported by a prior surface reflectance database. A monthly synthesis surface reflectance database was created using the 8 day synthetic MODIS surface reflectance product (MOD09A1) to provide the surface reflectance for cloud detection, and a dynamic thresholds model related to the land surface reflectance, observation geometry, and other parameters was developed based on the simulated relations between the apparent reflectance and the surface reflectance using the 6S (the Second Simulation of the Satellite Signal in the Solar Spectrum) model [Vermote et al., 1997; Kotchenova et al., 2006]. This method effectively improved cloud detection accuracy, particularly for the detection of broken and thin clouds.

The data obtained from MODIS and Landsat 8 OLI (Operational Land Imager) were used for the cloud detection experiment with the UDTCDAD method in this paper. The MODIS sensor operates on both the Terra and Aqua spacecraft, which were successfully launched in December 1999 and May 2002, respectively. The MODIS has a viewing swath width of 2330 km and monitors the surface of the Earth every 1 to 2 days. Its detectors measure 36 spectral bands between 0.4 and 14 μm, and the MODIS acquires data at three spatial

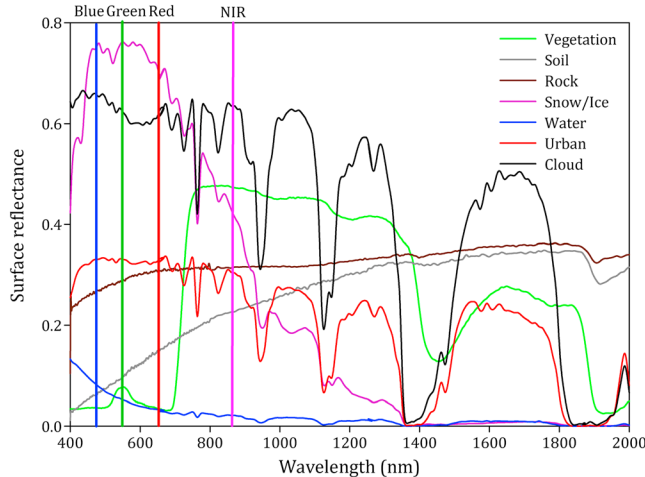


**Figure 1.** Spectra of typical objects.

water management, forest monitoring, and disaster monitoring. The following chapters successively detail the principles and methodology of the cloud detection algorithm, evaluation methods and the results.

## 2. Principles

Figure 1 shows the spectra of typical features, including vegetation, soil, rock, water, and snow/ice, which were collected from the ASTER spectral library. The ASTER spectral library is a compilation of over 2400 spectra of natural and manmade materials and was released on 3 December 2008. The library includes data from three other spectral libraries: the Johns Hopkins University Spectral Library, the Jet Propulsion Laboratory Spectral Library and the United States Geological Survey Spectral Library [Baldridge *et al.*, 2009]. Moreover, the spectra of urban areas and clouds were collected from the Airborne Visible Infrared Imaging Spectrometer, a hyperspectral data sensor with 224 spectral bands covering a spectral range of 0.4–2.5  $\mu\text{m}$  with a spectral resolution of 10 nm [Wei *et al.*, 2015].

Figure 1 shows that the reflectance of the cloud is much higher for most typical objects, including vegetation, water, soil, rock, and urban areas, except snow/ice, particularly in short wavelengths. The reflectance in the visible wavelength of vegetation, soil, and water is less than 0.2; however, because the cloud reflectance is greater than 0.6, the traditional methods of cloud detection have generally used a fixed threshold in such wavelengths to differentiate the cloudy pixels from the clear sky, such as the ISCCP, APOLLO, and the CLAVR. In addition to the visible bands, the bands of near infrared and short-wave infrared were used to detect clouds because of differences in the reflectance of clouds and other objects. To separate the clouds from other objects, a combination of two or more bands was also used for cloud detection, such as the Sand Dust Index [Hai *et al.*, 2009] to differentiate sand from clouds and the Difference Snow Index or Ratio Snow Index [Lin *et al.*, 2012] to separate snow from clouds.

Figure 1 shows that the reflectance is much different between a cloud and typical land objects at certain wavelengths; thus, traditional methods separate the cloudy pixels from the clear pixels. In fact, the reflectance of the satellite data is much more complex than the reflectance of the data shown in Figure 1. In Figure 1, the reflectance only represents the component reflectance in one pixel; however, it is well known that mixed pixels are ubiquitous in remote sensing images. Mixed pixels are a combination of more than one distinct substance. If a pixel is pure pixel, having only one object, the reflectance is nearly identical to the reflectance of the identical object measured on land, as shown in Figure 1. A mixed pixel may comprise water and vegetation or soil and snow; a mixed pixel may also comprise water and broken or thin clouds. The reflectance of a mixed pixel is determined by all of the components in the pixel and can be described by a linear equation [Keshava and Mustard, 2002]:

$$P = \sum_{i=1}^N c_i e_i + n = Ec + n, \quad \sum_{i=1}^N c_i = 1 \quad (1)$$

resolutions: 250 m, 500 m, and 1000 m. Many parameters can be derived from MODIS observations to describe features of the land, oceans, and the atmosphere, and these parameters can also be used for studies of processes and trends on local and global scales. The Landsat 8 satellite is the eighth satellite of the land survey satellite series of the United States, successfully launched by NASA in February 2013. Landsat 8 OLI is one of two sensors on Landsat 8 and images the entire Earth every 16 days. Landsat 8 OLI has eight multispectral bands with a spatial resolution of 30 m and has been widely used in different fields, including agriculture,

where  $P$  is the reflectance of the pixel,  $N$  is the number of the components in it,  $e_i$  is the reflectance of each component,  $c_i$  is the ratio of the area of  $e_i$ , and  $n$  is the value of uncertainty.

The difference between the cloud and the land objects shown in Figure 1 only represents a thick cloud and a pure land object. However, in most cases, the cloudy pixels are covered by thin or broken clouds instead of thick clouds. Thus, the reflectance of the pixel results from the cloud and the land objects together, which can be calculated using equation (1). The reflectance difference between the cloudy pixels and the land object is not as obvious as in Figure 1. In the visible wavelengths, the reflectance of a pixel covered by thin cloud over soil may be lower than the reflectance of the rock pixel, as occurred in the short-wave infrared bands when differentiating pixels of cloud over water from vegetation. The complex land structures rendered it impossible to obtain a proper threshold to separate the cloudy pixels from the clear sky. Traditional methods of cloud detection can accurately detect a thick cloud yet often fail to detect thin or broken clouds, particularly in low reflectance areas. Even for a satellite with many bands, such as MODIS, which uses 22 selected bands from a total of 36 bands for cloud detection, the uncertainty remains.

The traditional method uses a fixed threshold to identify all thin or broken clouds but occasionally misses the cloudy pixels of thin or broken clouds over the low surface reflectance areas or falsely identifies high-reflectance land objects as clouds. The surface reflectance of water, rock, and clouds are 0.05, 0.35, and 0.6 in the red band (approximately at  $0.66 \mu\text{m}$ ), respectively (Figure 1). According to equation (1), when the area ratio of the thin or broken clouds over a water pixel reaches approximately 40%, the reflectance is approximately 0.27, which is lower than the reflectance of rock. If the threshold is set at greater than 0.35, the pixels with an area ratio of thin or broken clouds of less than 40% over water areas will be missed; however, if the threshold is set lower than 0.35, the clear pixels covered by rock will be mistaken for cloud.

The difficulty in differentiating real land surface from clouds is a primary reason for the failure of thin or broken cloud detection with high precision from satellite data. In such circumstances, it is difficult to determine the appropriate threshold with which to identify clouds. If the reflectance is known prior to cloud detection, the component of underlying surfaces in mixed pixels can be determined and the thresholds can be established according to the real land surface reflectance. Thus, thin or broken clouds over water can be differentiated from clear pixels with relatively high accuracy with a threshold of reflectance greater than 0.05, and the rock pixel will be identified as a clear pixel even if the reflectance reaches 0.35.

Focusing on the above problem, a new dynamic threshold cloud detection algorithm with prior surface reflectance support was proposed to improve the accuracy of cloud detection. The surface reflectance is created using the current MODIS surface reflectance products to provide the real surface reflectance for the image to be detected, and then dynamic thresholds related to surface reflectance for cloud detection can be estimated based on the radiative transfer model.

### 3. Methodology

#### 3.1. Surface Reflectance Database Construction

MOD09A1 data were selected to represent the land surface reflectance supply for the database. The MOD09A1 data set is the 8 day gridded Level 3 product of the MOD09 series of surface reflectance and includes seven bands covering the visible to near-infrared wavelengths at a spatial resolution of 500 m. The MOD09A1 product provides the best possible L2G observations during an 8 day period, and the observations are selected on the basis of high observation coverage, low view angle, absence of clouds, or cloud shadows and aerosol loading, which effectively reduces the effect of surface and cloud contamination. The atmospheric correction accuracy is  $\pm(0.005 + 0.05 \times \rho)$  under favorable conditions [Vermote and Vermeulen, 1999; Vermote and Kotchenova, 2008].

In UDTCD, we assumed that the surface reflectance of most features remains unchanged during a certain period [Levy *et al.*, 2013; Sun *et al.*, 2016]. Therefore, a monthly surface reflectance database was created using the Minimum Synthesis Technology for cloud detection for that month. The lowest surface reflectance for each pixel of four images from a given month was chosen to be the pixel for the 1 month series to reduce the effects of cloud and surface contamination,

$$I(i,j) = \text{Min}(I_1(i,j), I_2(i,j), I_3(i,j), I_4(i,j)) \quad (2)$$

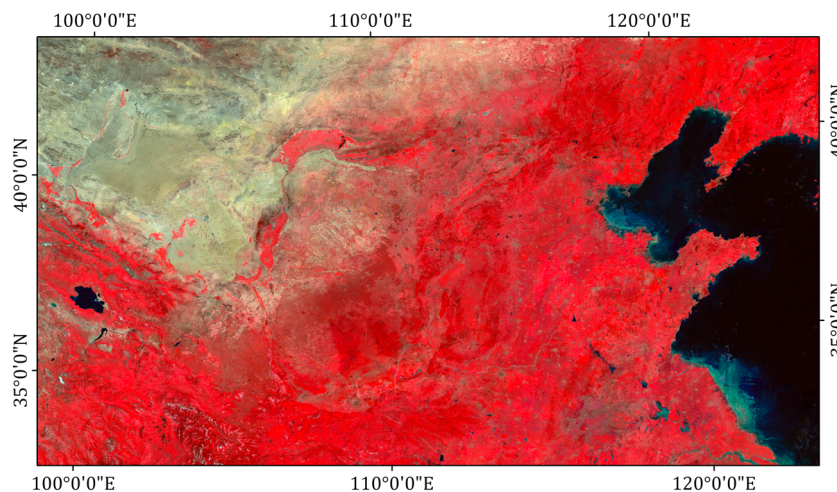


**Figure 2.** False standard color composite image (RGB: 214) of a surface reflectance image in July 2014.

where  $I$  represents the synthetic image;  $I_1, I_2, I_3$ , and  $I_4$  represent four MOD09A1 images in a month; and  $i$  and  $j$  represent the row and column, respectively, in an image.

MOD09A1 products for the entire year from 2013 to 2014 were collected and processed to construct the prior surface reflectance database. The surface reflectance images included the blue (0.459–0.479  $\mu\text{m}$ ), green (0.545–0.565  $\mu\text{m}$ ), red (0.620–0.670  $\mu\text{m}$ ), and near-infrared (0.841–0.876  $\mu\text{m}$ ) bands with a spatial resolution of 500 m for Landsat 8 OLI and resampled to 1 km spatial resolution using the bidirectional linear interpolation method for MODIS. Figure 2 shows the false standard color composite image (RGB: band2-band1-band-3) of a partial surface reflectance image in Asia (30°–45°N, 100°–125°E) from the synthetic surface reflectance database in July 2014 for demonstration. The surface reflectance images can better reflect the land cover type changes and show an overall high quality with less cloud cover, which can provide the actual surface reflectance for underlying surfaces.

### 3.2. Estimation of Dynamic Thresholds for Cloud Detection

The estimation of the dynamic thresholds is a key step for cloud detection. Unlike the fixed thresholds in traditional cloud methods, the thresholds used here are related to the real land surface reflectance; thus, the thresholds are called dynamic thresholds. The following work is included in the thresholds estimate: (1) band selection for the cloud detection, (2) analyzing the factors that may affect the relation between cloud and clear pixels, and (3) estimation of dynamic thresholds for cloud detection.

#### 3.2.1. Band Selection

The greatest difference between the cloud and most land objects is in the wavelengths of visible to near infrared (NIR) (Figure 1). Thus, the visible-to-NIR bands—bands 1, 2, 3, and 4 of the MODIS and bands 2, 3, 4, and 5 of Landsat 8 OLI—were chosen for cloud detection of the two satellite data. To differentiate snow/ice from cloud, short-wave infrared bands—bands 7 of MODIS and band 6 of Landsat 8 OLI—were also chosen for the obvious reference difference between cloud and snow/ice. Table 1 shows the detailed parameters for the chosen bands.

**Table 1.** Detailed Parameters of the Chosen Bands for MODIS and Landsat 8

MODIS			Landsat 8		
Bands	Channel	Wavelength	Bands	Channel	Wavelength
Band 1	Red	0.620–0.670	Band 2	Blue	0.450–0.515
Band 2	NIR	0.841–0.876	Band 3	Green	0.525–0.600
Band 3	Blue	0.459–0.479	Band 4	Red	0.630–0.680
Band 4	Green	0.545–0.565	Band 5	NIR	0.845–0.885
Band 7	SWIR	1.628–1.652	Band 6	SWIR	1.560–1.660

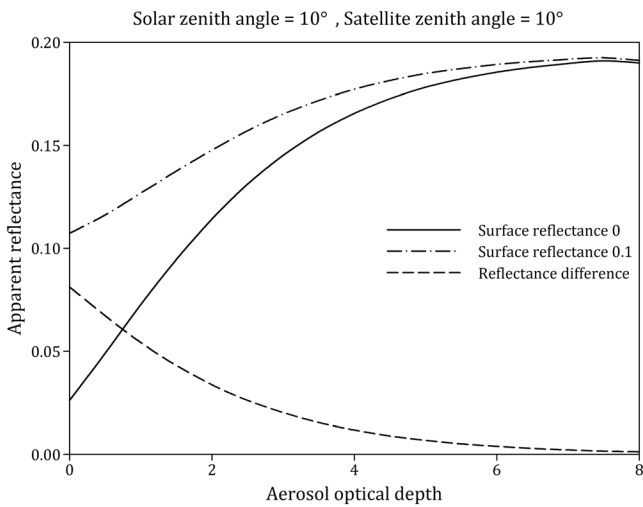


**Figure 3.** Relationship between apparent reflectance and AOD under different surface reflectances.

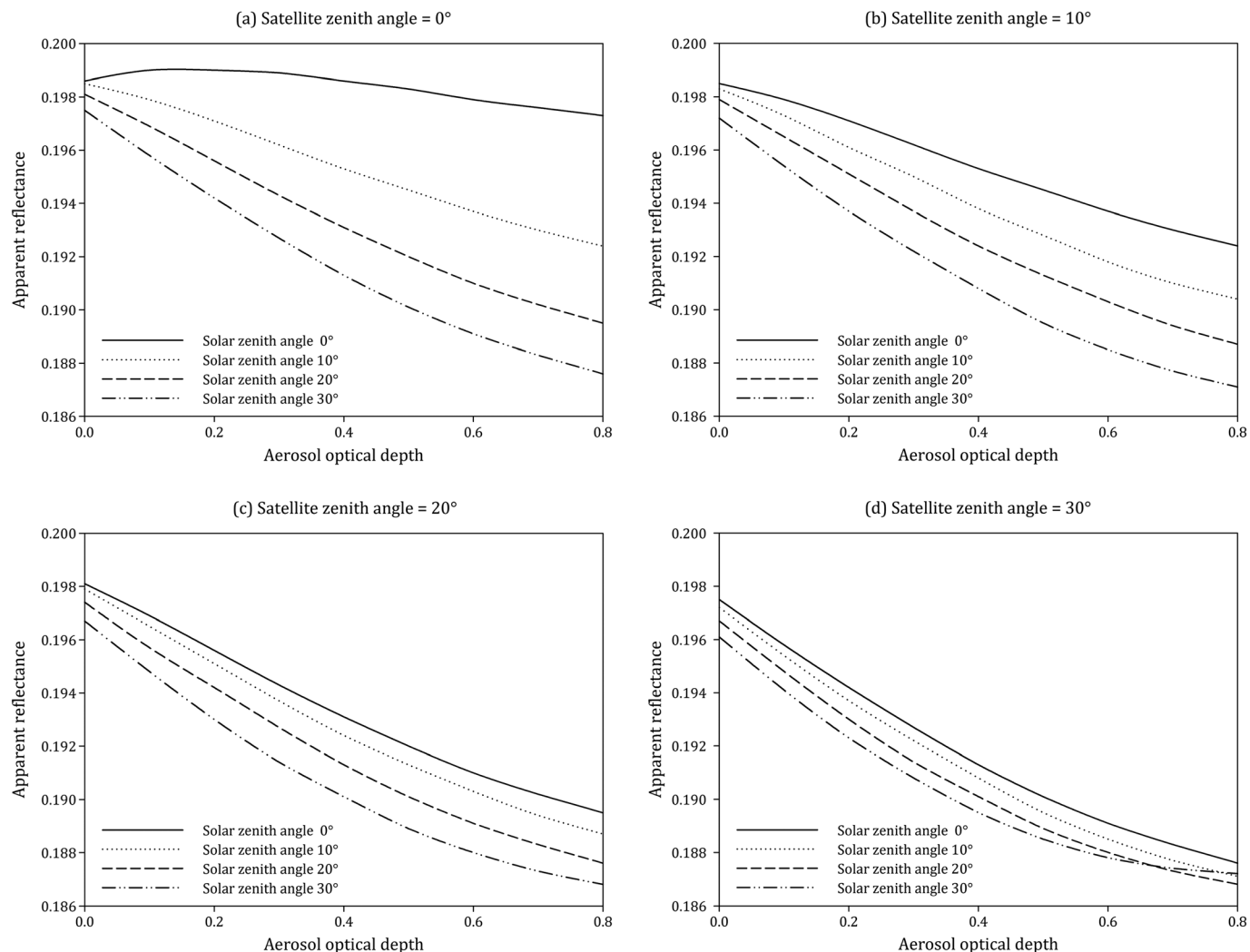


**Figure 4.** Relationships between apparent reflectance and AOD with respect to different geometric parameters.

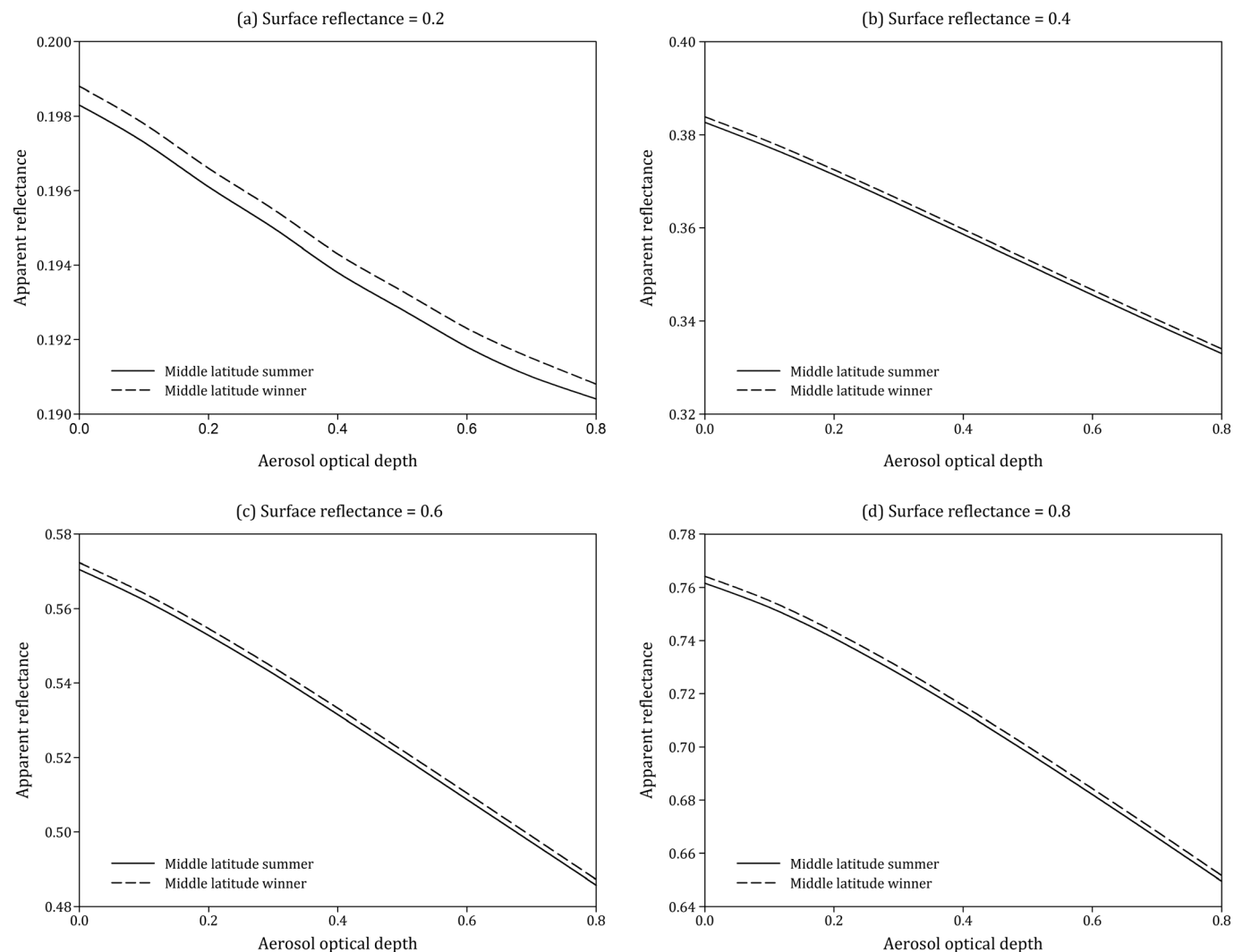


**Figure 5.** Relationships between apparent reflectance and AOD under different atmospheric models.

transfer code used for simulations of satellite observation under clear-sky conditions that carefully considers elevated targets, molecular and aerosol scattering, and gaseous (including  $\text{H}_2\text{O}$ ,  $\text{O}_3$ ,  $\text{O}_2$ , and  $\text{CO}_2$ ) absorption [Vermote *et al.*, 1997; Kotchenova *et al.*, 2006]. Observation parameters such as spectral response function, observation, and geometric parameters; and atmospheric parameters such as observation, geometric, atmospheric, and aerosol models; and AOD were input into the simulations using the 6S model. Therefore, the relations between apparent reflectance and surface reflectance under different conditions can be simulated. In this paper, the red band ( $0.65 \mu\text{m}$ ) of Landsat 8 was selected to perform simulation experiments for demonstration.

### 3.2.2.1. Aerosol Optical Depth

Figure 3 shows the simulated relation between apparent reflectance and the AOD with different surface reflectance values of 0.0 and 0.1. The solar and satellite zenith angles were set to a fixed value of  $10^\circ$ . The simulated results showed the apparent reflectance clearly increasing with the increase in the AOD and saturation when the AOD reached 6. In the current study, the maximum AOD was set at 0.8 in the simulation experiments of parameters under most clear-sky conditions except in extreme weather such as fog or dust [Remer *et al.*, 2006].

### 3.2.2.2. Geometric Parameters

The observation geometry that affects the reflectance includes the solar zenith angle, the view zenith angle, and the relative azimuth angle between the Sun and the satellite. Figure 4 shows the simulated relations

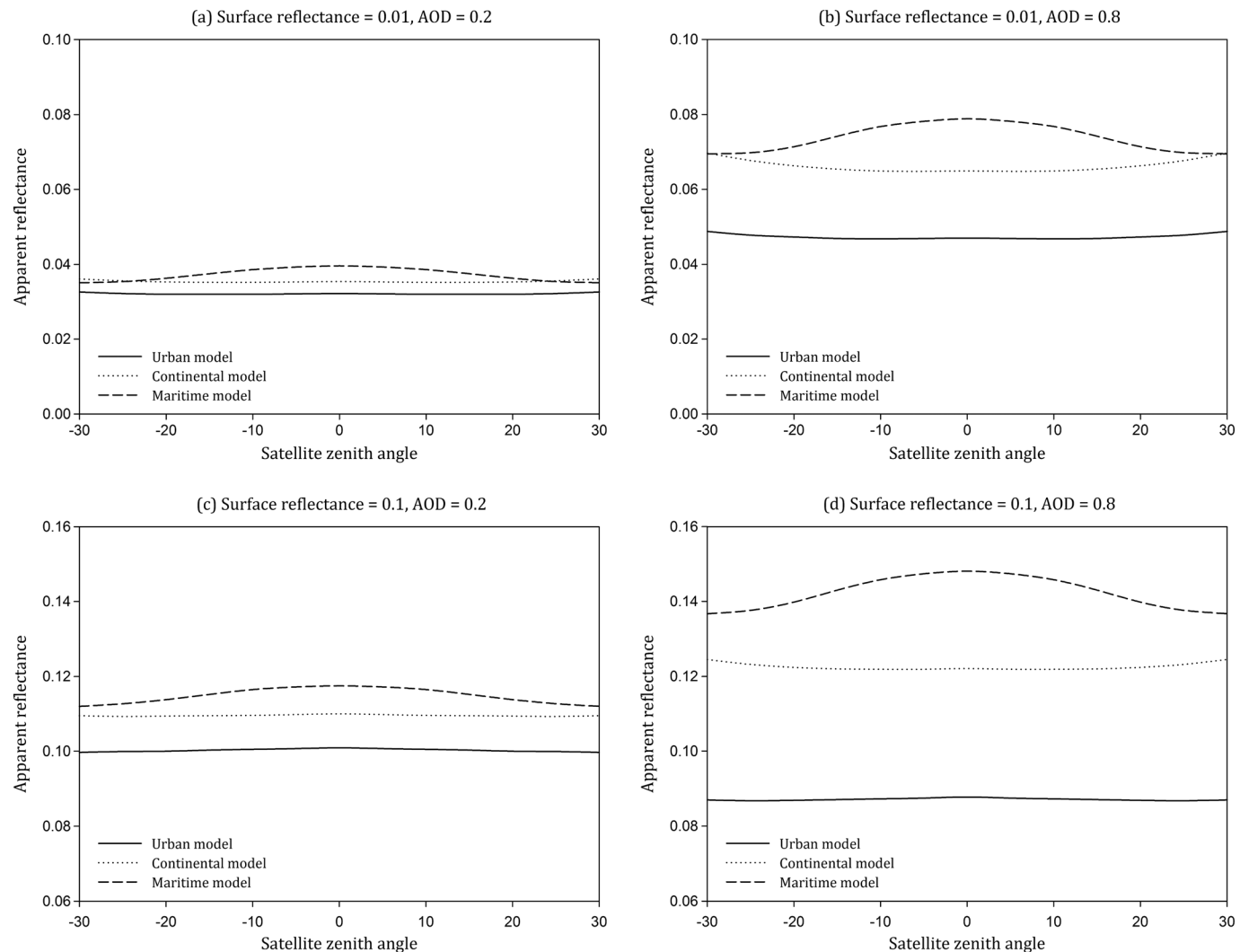


**Figure 6.** Relationships between apparent reflectance and geometric parameters under different aerosol models.

between apparent reflectance and the AOD with the changes in solar and satellite zenith angles. The surface reflectance was 0.2; the solar and satellite zenith angles were 0°, 10°, 20°, and 30°; and the AODs ranged from 0.0 to 0.8 with an interval of 0.1. As shown in Figure 4, the apparent reflectance decreased with an increasing AOD, although there were certain differences between the apparent reflectance and the AOD within different geometric parameters.

### 3.2.2.3. Atmospheric Model

Figure 5 shows the simulated relation between apparent reflectance and the AOD in different atmospheric models. The two typical atmospheric models—middle-latitude summer and middle-latitude winter—were selected for simulation experiments. The surface reflectance was 0.2, 0.4, 0.6, and 0.8; the solar and satellite zenith angles were 30° and 20°; and the AODs ranged from 0.0 to 0.8 with an interval of 0.1. The simulated results show that the apparent reflectance presented a clear decreasing trend with an increasing AOD and that the difference in apparent reflectance decreased when surface reflectance increased in different atmospheric models (approximately 0.01–0.03), which may explain why atmospheric models exhibit little effect on apparent reflectance.

### 3.2.2.4. Aerosol Model

Figure 6 shows the simulated relation between apparent reflectance and satellite zenith angles in different aerosol models. The surface reflectance was set to 0.01 and 0.1, the AODs were set to 0.2 and 0.8, and the

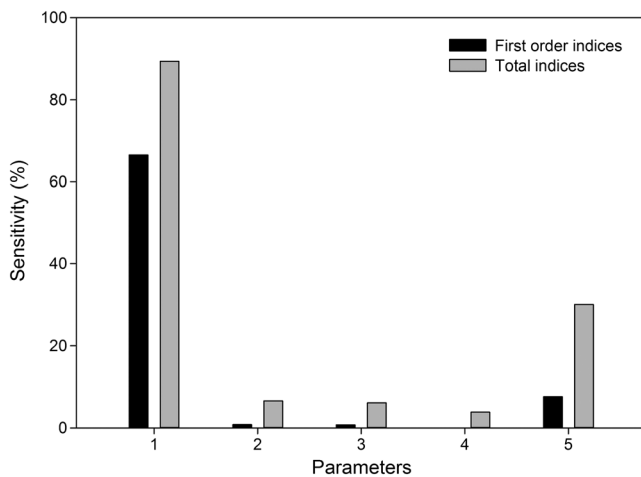


**Figure 7.** First-order and total-order indices of the sensitivity analysis (1 = aerosol optical depth, 2 = solar zenith angle, 3 = satellite zenith angle, 4 = atmospheric model, and 5 = aerosol model).

between the continental and urban aerosols exceeded 0.03, and the MAE between the continental and maritime aerosols exceeded 0.02. Therefore, aerosol models can cause a large difference and greatly affect apparent reflectance.

### 3.2.2.5. Sensitivity Analysis

To quantitatively analyze the effects of the above parameters on apparent reflectance, the EFAST (Extended Fourier Amplitude Sensitivity Test) method was selected and adopted for parameter sensitivity. The EFAST is a global and quantitative sensitivity analysis algorithm that can be applied to complex nonlinear and nonmonotonic models [Saltelli *et al.*, 1999, 2010]. The EFAST adopts the idea of model variance analysis and considers that the variance of model output is caused by interaction among input parameters, which can reflect the sensitivity of model output to input parameters. The first-order sensitivity index is the sensitivity of a single parameter independent of the model results, and the total sensitivity index also includes the effect of the coupling of different parameters on the results of the model. The total- and first-order sensitivity indices of each parameter are obtained via an analysis of the impacts of the input factors on the output variance. Because of its robust and efficient characteristics, the EFAST is used to analyze global sensitivity via variance decomposition and is widely used in quantitative evaluation and uncertainty analysis in hydrological, ecological and meteorological modeling [Cukier *et al.*, 1973; Varella *et al.*, 2010; Miao *et al.*, 2011; Saltelli *et al.*, 1999; Pandya *et al.*, 2012]. Five parameters—*aerosol optical depth*, *solar zenith angle*, *satellite zenith angle*, *the atmospheric model*, and *the aerosol model*—were selected to evaluate the contribution to apparent reflectance using the EFAST method.

Figure 7 shows the sensitivity analysis of the effects of observation and atmospheric factors on apparent reflectance. Sensitivity analysis results showed that *aerosol optical depth* has a greater effect on apparent reflectance with higher first-order and total-order indices. The *aerosol model* also has a great effect on apparent reflectance because the *aerosol model* is one of the primary factors affecting regional aerosol. In addition, the *atmospheric model* and *geometric parameters* indicate relatively small but certain effects on the apparent reflectance. Therefore, atmospheric and observational factors can cause obvious differences between the surface reflectance and the apparent reflectance and must be carefully considered when establishing cloud detection models.

### 3.2.3. Estimation of Dynamic Thresholds

The 6S model was used to simulate the influence of the above factors on the apparent reflectance. Figure 8 shows the simulated relations of the apparent reflectance changing according to the land surface reflectance variation in an AOD of 0.2, 0.4, 0.6, and 0.8 and a satellite zenith of 0°, 10°, 20°, and 30°, respectively. The *aerosol model* was set to the *continental model*, and the *atmospheric model* was *middle-latitude summer*. The results indicate that the apparent reflectance exhibits certain differences with different AODs, and the changing speeds are much different; when the land surface reflectance is lower than 0.05 or greater than 0.4, the difference is greater.

sun zenith angle was set to a fixed value of 30°. Three aerosol models—the *urban model*, the *maritime model*, and the *continental model*—were chosen for the simulation experiment.

The simulated results showed that the differences between the apparent reflectance and the zenith angles are smaller when the AOD is small in different aerosol models. The mean absolute error (MAE) of apparent reflectance between continental and urban aerosol was less than 0.005, and the MAE between the continental and maritime aerosols was less than 0.01. However, when the AOD increased, the MAE of apparent reflectance in different aerosol models clearly increased. The MAE

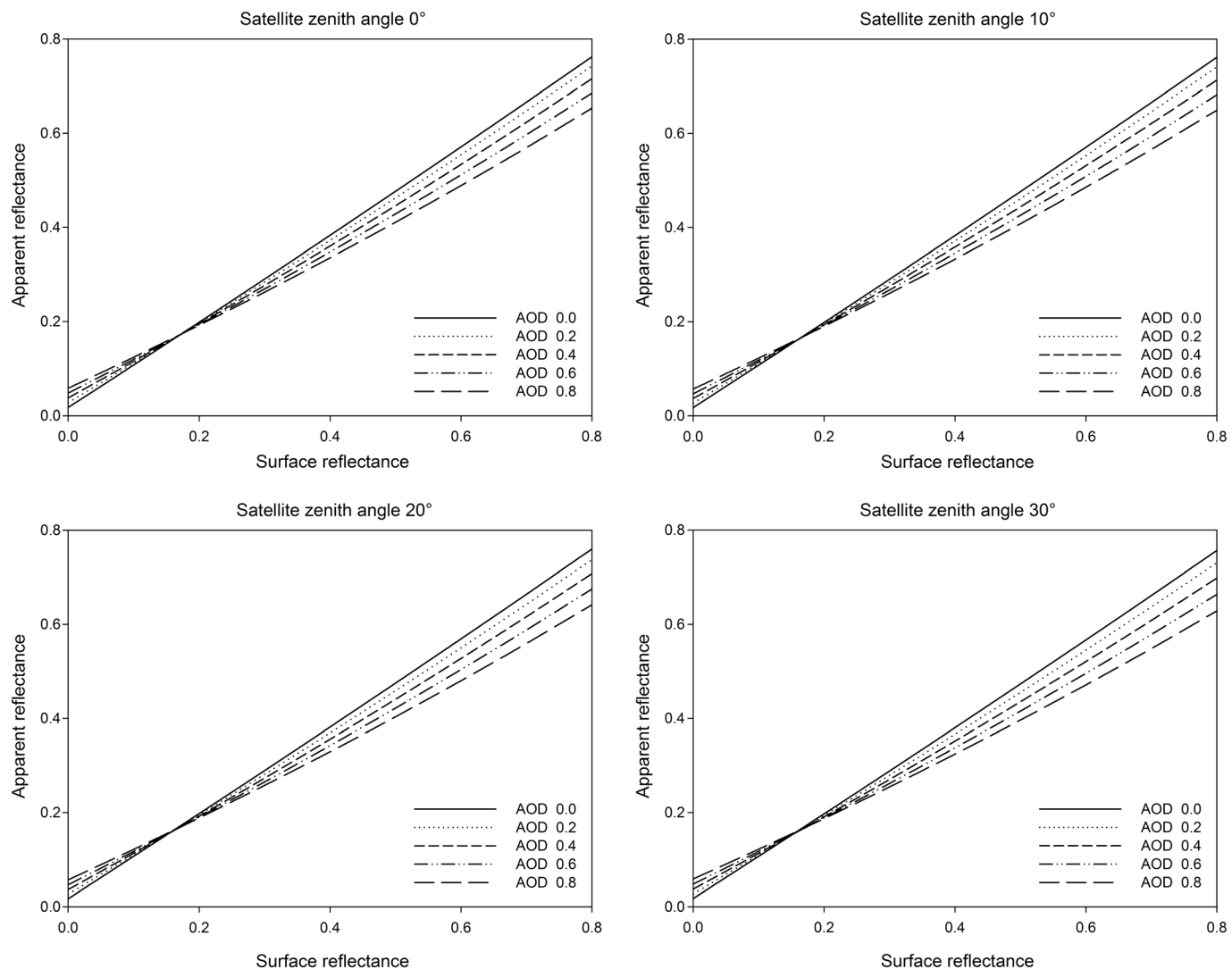


**Figure 8.** Simulated relationships between apparent reflectance and surface reflectance.

Using dynamic thresholds based on the prior surface reflectance database is the primary characteristic of the UDTCDa to detect a cloud. In the new algorithm, we assumed that if the apparent reflectance of a pixel exceeded the maximum of the changing simulated apparent reflectance calculated with the changing surface reflectance under different observation and atmosphere conditions, this pixel would be identified as a cloudy pixel. The possible satellite apparent values of the four bands of MODIS and Landsat 8 OLI, with different land surface reflectance values, were calculated with the 6S model. Solar and satellite zenith angles covered all possible values of the two types of satellite sensors used in this work. The maximum values of apparent reflectance distribution can be simulated and the dynamic thresholds of simulated apparent reflectance can be determined as a function of surface reflectance and observation geometry under possible atmospheric conditions without clouds. Equations 3–10 show the corresponding dynamic threshold cloud detection models for MODIS and Landsat 8 OLI data. The cloud detection rules for the MODIS data are as follows:

$$\rho_B^{*'} = 0.793 \cdot \rho_B + 0.004 \cdot \cos\alpha \cos\beta + 0.158 \quad (3)$$

$$\rho_G^{*'} = 0.807 \cdot \rho_G + 0.025 \cdot \cos\alpha \cos\beta + 0.125 \quad (4)$$

$$\rho_R^{*'} = 0.843 \cdot \rho_R + 0.017 \cdot \cos\alpha \cos\beta + 0.112 \quad (5)$$

$$\rho_{TIR}^{*'} = 0.928 \cdot \rho_{NIR} + 0.010 \cdot \cos\alpha \cos\beta + 0.099 \quad (6)$$

The cloud detection rules for the Landsat 8 OLI data are as follows:

$$\rho_B^{*'} = 0.834 \cdot \rho_B + 0.025 \cdot \cos\alpha \cos\beta + 0.143 \quad (7)$$

$$\rho_G^{*'} = 0.882 \cdot \rho_G + 0.040 \cdot \cos\alpha \cos\beta + 0.097 \quad (8)$$

$$\rho_R^{*'} = 0.912 \cdot \rho_R + 0.049 \cdot \cos\alpha \cos\beta + 0.108 \quad (9)$$

$$\rho_{\text{TIR}}^{*'} = 0.940 \cdot \rho_{\text{NIR}} + 0.010 \cdot \cos\alpha \cos\beta + 0.189 \quad (10)$$

The dynamic threshold method cloud detection rules are as follows:

$$R_i = \rho_i^* - \rho_i^{*'} > 0, i = B, G, R, \text{NIR} \quad (11)$$

$$R = R_B \cup R_G \cup R_R \cup R_{\text{NIR}} \quad (12)$$

where  $\rho_i^{*'}$  represents the simulated apparent reflectance of different channels,  $\rho_i$  represents the surface reflectance,  $\alpha$  represents the solar zenith angle,  $\beta$  represents the satellite zenith angle,  $\rho_i^*$  represents the apparent reflectance,  $R_i$  represents the corresponding cloud detection results for each channel, and  $R$  represents the final cloud detection result.

### 3.3. Snow/Ice Identification

For similar spectral characteristics, snow/ice is difficult to differentiate from cloud with the four bands from visible to NIR channels used above. The greatest difference between these two types of objects lies in the wavelength of the short-wave infrared band (approximately at 1.6  $\mu\text{m}$ ), in which, although clouds still have a higher reflectance, the reflectance of ice and snow is nearly 0 (Figure 1). Therefore, the short-wave infrared band was selected to identify clouds and snow/ice. The Normalized Difference Snow Index (NDSI), calculated from a visible and a short-wave infrared band, was selected to distinguish and mask the snow/ice from the cloud. The NDSI is defined as

$$\text{NDSI} = (\rho_G - \rho_{\text{SWIR}}) / (\rho_G + \rho_{\text{SWIR}}) \quad (13)$$

where  $\rho_G$  represents the apparent reflectance of the green band (0.56  $\mu\text{m}$  for Landsat 8 and 0.55  $\mu\text{m}$  for MODIS) and  $\rho_{\text{SWIR}}$  represents the apparent reflectance of the short-wave infrared band (1.61  $\mu\text{m}$  for Landsat 8 and 1.64  $\mu\text{m}$  for MODIS [Salomonson and Appel, 2006]). When the NDSI  $> 0.4$ , the pixels are deemed snow or ice covered [Hall *et al.*, 1995, 2002; Klein and Barnett, 2003].

### 3.4. Spectral Correction for Landsat 8 OLI

Radiometric calibration is required for Landsat 8 OLI data, and the digital number can be converted to apparent reflectance using the reflectance rescaling factor coefficients in the header file [Sun *et al.*, 2016]. To conduct cloud detection experiments using Landsat 8 data with MOD09 surface reflectance product support, the spectral differences between the two sensors must be considered. Figure 9 shows the filter response function for MODIS and Landsat 8 OLI data from visible to near-infrared bands. The center wavelength of the four bands of Landsat 8 (0.483, 0.563, 0.655, and 0.865  $\mu\text{m}$ ) is close to the corresponding bands of MODIS (0.469, 0.555, 0.645, and 0.859  $\mu\text{m}$ ), although their bandwidths differ with the spectral responses.

Vegetation, water, and soil spectra ranging from 400 to 2500 nm with a spectral resolution of 1 nm were collected from the ASTER spectral library. The band reflectance was computed with the filter response functions of Landsat 8 OLI and MODIS according to equation (14):

$$R = \frac{\int_{\lambda_1}^{\lambda_2} S(\lambda) R(\lambda) d\lambda}{\int_{\lambda_1}^{\lambda_2} S(\lambda) d\lambda} = \frac{\sum_{i=0}^{N-1} S(\lambda_i) R(\lambda_i) \Delta\lambda}{\sum_{i=0}^{N-1} S(\lambda_i) \Delta\lambda} \quad (14)$$

where  $S(\lambda)$  is the filter response function and  $R(\lambda)$  is the spectral reflectance at the wavelength  $\lambda$ .

Figure 10 compares the surface reflectance between MODIS and Landsat 8 in different channels. Although the surface reflectance of Landsat 8 is more consistent with the surface reflectance of MODIS, certain differences between them remain. Therefore, the errors caused by the different filter response functions must be corrected.

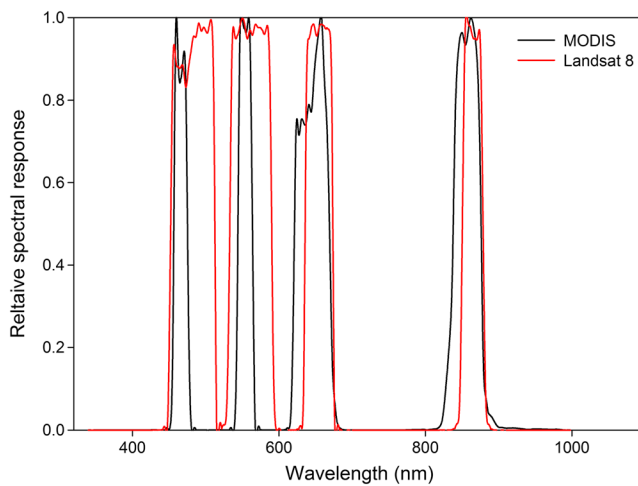


**Figure 9.** Spectral response curve comparison between MODIS and Landsat 8 data.

The linear relation between the surface reflectance of MODIS and Landsat 8 in different channels can be acquired in the form of equation (15). Thus, the errors from the filter response functions can also be corrected and analyzed (equation (16)):

$$r_{L8} = a \cdot r_{MODIS} + b \quad (15)$$

$$MD = \frac{|r_{L8} - r_{modis}|}{N} \quad (16)$$

where  $a$  and  $b$  are two linear fitting coefficients,  $r_{L8}$  is the surface reflectance of Landsat 8,  $r_{MODIS}$  is the surface reflectance of MODIS, MD is the mean difference, and  $N$  is the total number of samples.

Table 2 shows the linear analysis of the surface reflectance between the

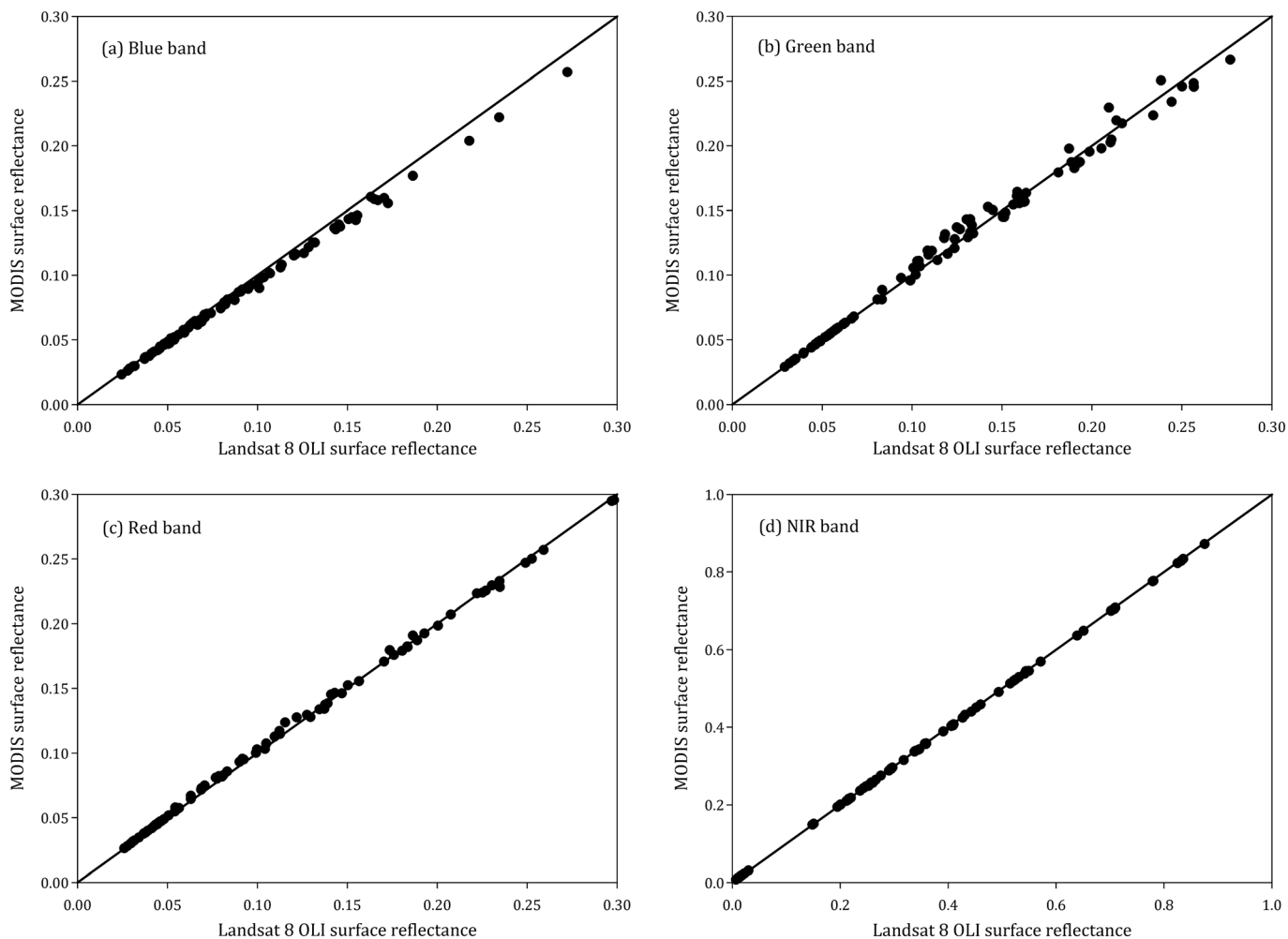


**Figure 10.** Comparison of land surface reflectance in different channels between Landsat 8 and MODIS.

**Table 2.** Linear Analysis of Land Surface Reflectance Values Between Landsat 8 and MODIS

Bands	$R^2$	a	b	Mean Difference (Before Correction)	Mean Difference (After Correction)
Blue band	0.9984	0.9389	0.0011	0.0042	0.0037
Green band	0.9912	0.9790	0.0042	0.0053	0.0018
Red band	0.9989	0.9864	0.0026	0.0023	0.0014
NIR band	0.9992	0.9956	0.0004	0.0018	0.0004

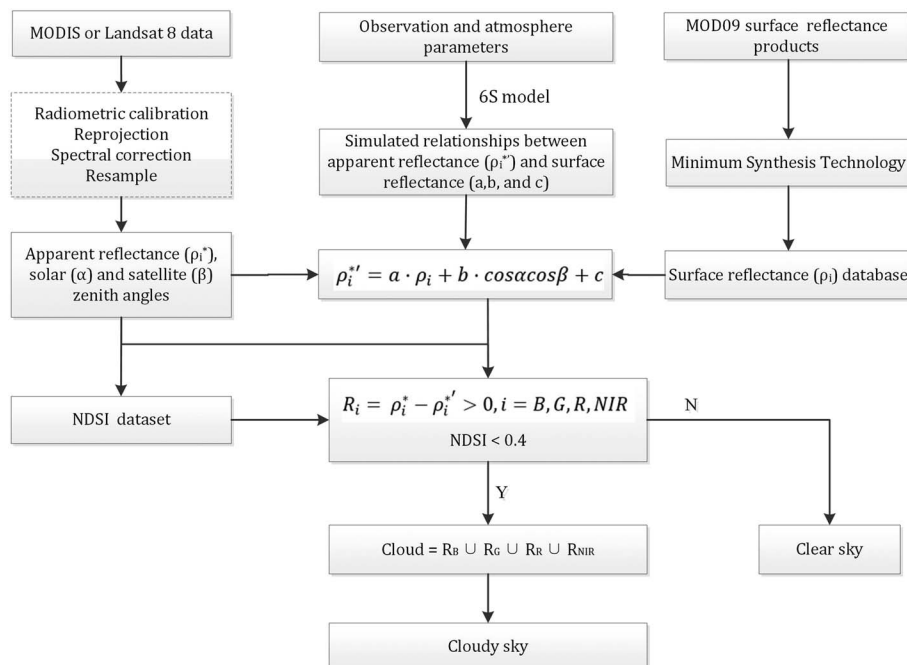
MODIS and Landsat 8 OLI data. Statistical results show that the mean difference was greatly reduced; the errors resulting from the spectral response functions were properly corrected. Figure 11 shows the flowchart of the UDTCDAs.

#### 4. Data Sources and Evaluation Methods

In this paper, Landsat 8 OLI and MODIS Level 1 calibrated radiance data at a 1 km spatial resolution (MOD021KM) were obtained and used to perform cloud detection experiments using the UDTCDAs. Moreover, the visual interpretation of clouds, the CALIPSO cloud product, and two MODIS cloud mask products, the MOD35 daily cloud mask product and the MOD04 daily aerosol product, were obtained for validation and comparison purposes.

##### 4.1. Visual Interpretation of Clouds

To examine the evaluation of cloud detection results quantitatively, the actual cloud information was extracted using remote sensing visual interpretation method. Based on the standard false-color composite image, the cloud distribution in the images was extracted via artificial quantification using the ArcGIS software. Then, the reference and estimated cloud mask products were generated through the vector to raster tool, resulting in a binary cloud mask (0 = cloud, 1 = clear) at a 1000 m spatial resolution. To reduce the effects of subjective or accidental errors, the cloud information from a total of 36 images from all the Landsat 8 and MODIS data we used in this paper was extracted. Figure 12 shows the visual interpretation results for broken, thick, and thin clouds extracted from the Landsat 8 OLI image as an example.

**Figure 11.** Flowchart of the UDTCDAs.

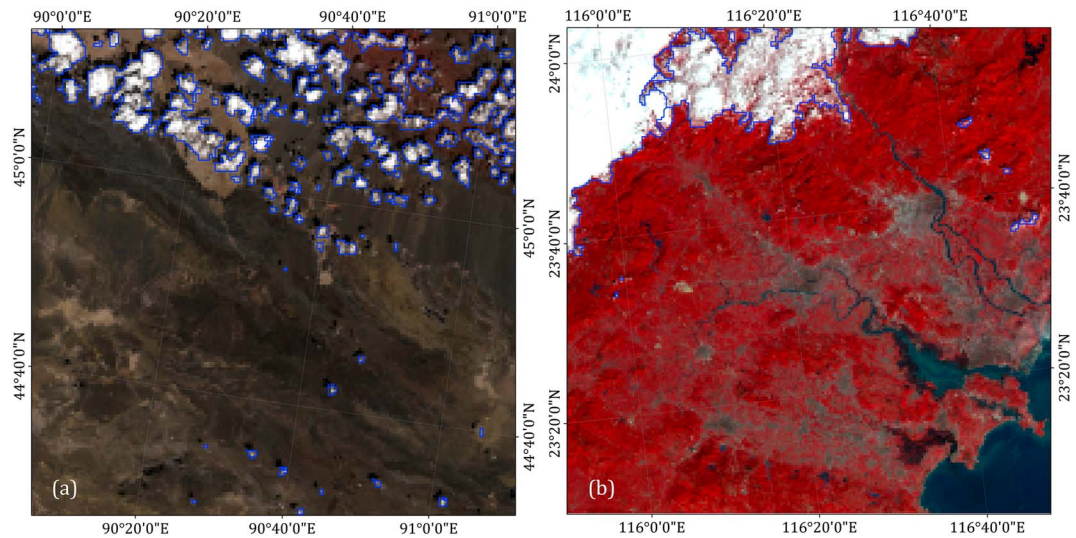


**Figure 12.** Visually interpreted cloud results for (a) broken and (b) thick and thin clouds.

#### 4.2. CALIPSO Cloud Product

CALIPSO is an environmental satellite constructed by the Cannes Mandelieu Space Center and was launched on 28 April 2006. CALIPSO follows a 705 km, circular polar orbit as part of the Aqua constellation and has a good collocation with the MODIS Aqua Satellite [Poole et al., 2002; Winker et al., 2010]. CALIPSO determines the cloud phase based on polarization information derived from ground-based depolarization Lidar. It provides nearly continuous, highly accurate measurements of the vertical structure and optical properties of clouds and aerosols and has substantially increased the understanding of the climate system and climate change. The Lidar level 2 cloud products are produced at three horizontal resolutions—1/3 km, 1 km, and 5 km—and have a temporal resolution of 16 days [Powell, 2005; Powell et al., 2009, 2013; Hu, 2007; Hu et al., 2009; Sassen et al., 2008; Chepfer et al., 2010]. In this paper, the Lidar level 2 cloud layer products with a spatial resolution of 1 km are selected for validation purposes.

#### 4.3. MODIS Cloud Mask Products

MOD35 is the MODIS Level 2 daily cloud mask product generated at 1 km and 250 m (at nadir) spatial resolutions. The MOD35 data are generated with the MODIS cloud mask algorithm and employs a series of visible and infrared thresholds and consistency tests to specify confidence that an unobstructed view of the Earth's surface is being observed [Ackerman et al., 2010; Remer et al., 2012]. The data set of "Cloud Mask: MODIS Cloud Mask and Spectral Test Results" at 1 km spatial resolution was selected for this paper.

MOD04 is the MODIS Level 2 daily aerosol product and has been updated to the Collection 6 (C6) version. The MOD04 C6 provides an overland cloud mask product that is a combination of tests using absolute magnitude and spatial variability at 0.47  $\mu\text{m}$  (500 m resolution) and 1.38  $\mu\text{m}$  (1 km resolution). The final result is a binary cloud mask at 500 m resolution used to filter pixels for final aerosol retrieval [Levy et al., 2013]. The data set of

**Table 3.** A Summary of the Research Data

Products	Version	Parameter	Original Resolution	Used Resolution	Time Series
MOD/MYD021KM	C6	Radiance Sensor Zenith Solar Zenith	1000 m	1000 m	2013 to 2014
MOD09A1	C6	Surface reflectance Surface reflectance	500 m 500 m	500 m 1000 m	2013 to 2014 2013 to 2014
MOD/MYD35	C6	Cloud mask	1000 m	1000 m	2013 to 2014
MOD/MYD04	C6	Cloud mask	500 m	1000 m	2013 to 2014
Landsat 8 OLI	-	Radiance	30 m	500 m	2013 to 2015
CALIPSO	-	Cloud	1000 m	1000 m	2013 to 2014

"Aerosol Cloudmask Land Ocean: Aerosol Cloud Mask 500 m resolution 0 = cloud 1 = clear" at 500 m spatial resolution was selected and resampled into a 1 km resolution using the bidirectional linear interpolation method in this paper. Detailed research data are shown in Table 3.

#### 4.4. Evaluation Methods

In the current study, the cloud amount (CA, equation (17)) was selected to reflect the total cloud content in the remote sensing image, and the cloud amount error (CAE, equation (18)) shows the error difference between the reference and estimated cloud amounts. A CAE greater than 0 indicates an overestimation, and a CAE less than 0 indicates an underestimation. In addition, the correct rate of cloudy pixels (CR, equation (19)), the correct rate of clear-sky pixels (SR, equation (20)), the error rate (ER, equation (21)), and the missing rate (MR, equation (22)), four typical evaluation indices, were selected to evaluate the cloud detection results at the pixel level:

$$CA = \frac{N_{\text{cloud}}}{N} \quad (17)$$

$$CAE = CA_{\text{product}} - CA_{\text{real}} \quad (18)$$

$$CR = \frac{TP}{N_{\text{real-cloud}}} \quad (19)$$

$$SR = \frac{TN}{N_{\text{real-clear}}} \quad (20)$$

$$ER = \frac{FP}{N_{\text{real-clear}}} \quad (21)$$

$$MR = \frac{FN}{N_{\text{real-cloud}}} \quad (22)$$

where  $N_{\text{cloud}}$  represents the total cloudy pixels and  $N$  represents the total pixels of the image;  $CA_{\text{product}}$  and  $CA_{\text{real}}$  represent the cloud amount of cloud mask product and the reference cloud mask, respectively;  $N_{\text{real-cloud}}$  represents the total cloudy pixels;  $N_{\text{real-clear}}$  represents the total clear-sky pixels in the reference cloud mask data; TP (true positive) represents the total number of pixels identified as cloudy pixels in both reference data and cloud detection results; TN (true negative) represents the total pixels identified as clear-sky pixels in both reference data and cloud detection results; FP (false positive) represents the total number of pixels identified as clear-sky pixels in reference data but cloudy pixels in cloud detection results; and FN (false negative) represents the total number of pixels identified as cloudy pixels in reference data but clear-sky pixels in cloud detection results.

## 5. Results and Discussion

MODIS and Landsat 8 OLI data cover different cloud types over different land use types in the years 2013 to 2015 were collected and utilized in cloud detection experiments using the UDTCD. For evaluation and comparison purposes, cloud detection results covering different cloud types, including broken, thick, and thin clouds over different surface types (e.g., vegetation, water, bare land, and desert), as determined using Google Earth with areas of interest 400 × 400 pixels in size, were randomly selected from both MODIS and Landsat 8 OLI data.

### 5.1. Evaluation of the UDTCD Cloud Mask for Landsat 8 OLI

Figure 13 shows the UDTCD cloud detection results of Landsat 8 data for demonstration, in which Figures 13a–13d represent the broken cloud detection results, Figures 13e–13h represent the thick and thin cloud detection results, and Figures 13i–13l represent the cloud detection results of different cloud types over bright areas. Table 4 shows the corresponding evaluation of the cloud detection results of Landsat 8 shown in Figure 13.

Broken clouds are generally small plaques covered with a small quantity of cloud with a clear fixed edge in the image. Fixed threshold methods demonstrate poor detection accuracy on edges and the scattered punctate of broken clouds with large omission errors. However, broken clouds over different surfaces (including vegetation and water areas) are better detected with the UDTCD (Figures 13a–13d).

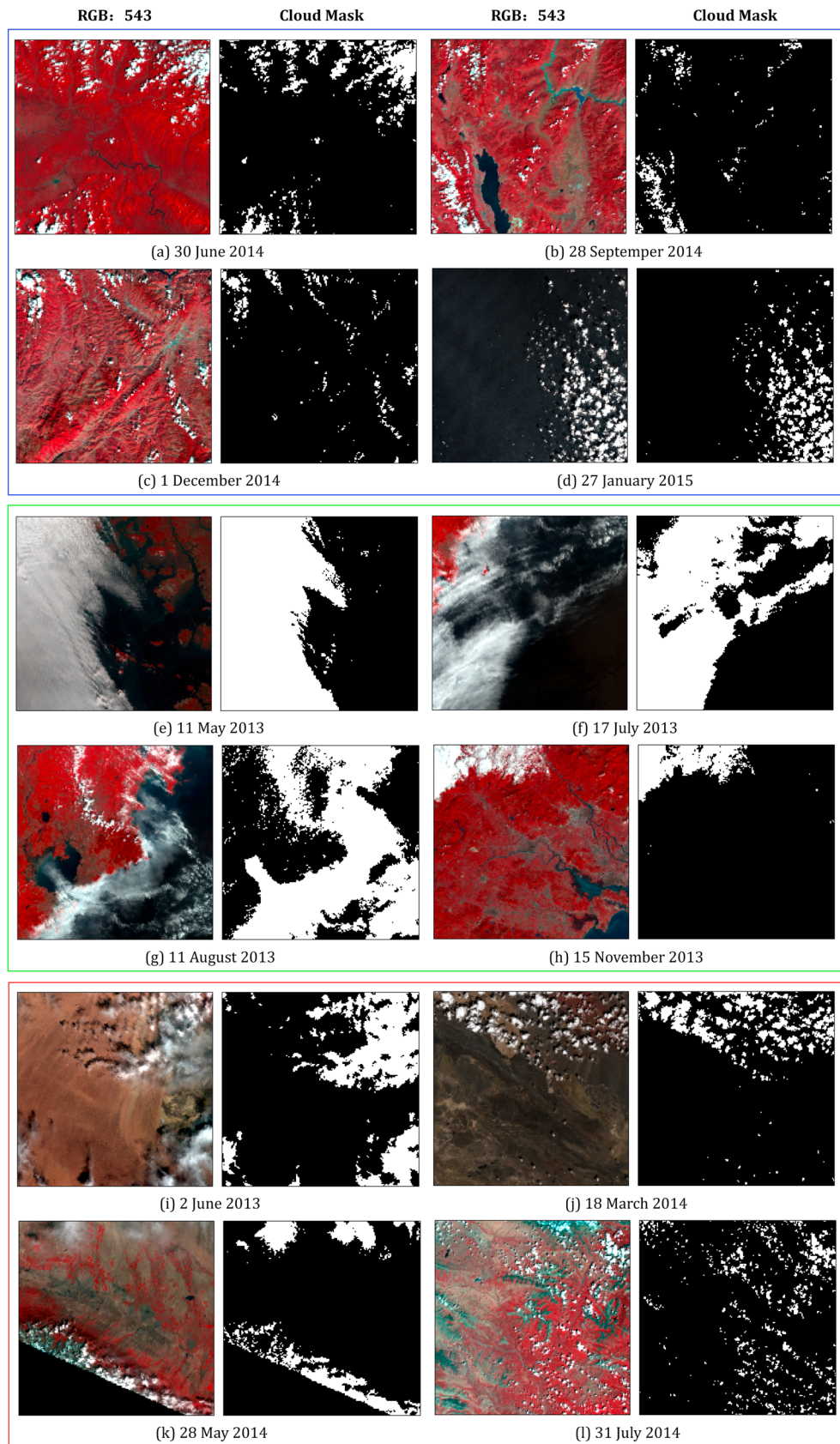


Figure 13. UDTCDa cloud detection results for different cloud types over different regions based on Landsat 8 data.

**Table 4.** Evaluation of UDTCD Cloud Detection Results Based On Landsat 8 Data

Cloud Types	No.	CA <sub>real</sub> (%)	CA <sub>new</sub> (%)	MAE (%)	CR (%)	ER (%)	MR (%)	SR (%)	Land cover
Broken cloud	a	13.80	13.15	-0.66	97.62	7.46	2.38	92.54	Vegetation
	b	6.05	5.45	-0.60	85.21	0.31	14.79	99.69	Vegetation
	c	4.91	4.33	-0.58	80.48	0.40	19.52	99.60	Water
	d	9.94	8.65	-1.29	80.10	0.76	19.90	99.24	Water
Thick and Thin cloud	e	51.33	49.97	-1.36	96.70	0.68	3.30	99.32	Water
	f	57.26	58.38	+1.12	95.20	8.83	4.80	91.27	Vegetation and Water
	g	50.31	50.12	-0.19	92.19	7.53	7.81	92.47	Vegetation and Water
	h	12.95	11.10	-1.85	95.07	0.04	4.93	99.96	Vegetation
Bright areas	i	10.48	11.91	+1.43	90.26	2.74	9.74	97.26	Desert
	j	6.48	6.62	+0.14	93.48	0.60	6.52	99.40	Desert
	k	10.70	10.52	-0.18	85.75	1.51	14.25	98.49	Bare land
	l	8.94	8.87	-0.06	82.65	1.63	17.35	98.37	Bare land

Evaluation results showed that the UDTCD had better cloud detection accuracy with lower CAE (~0.58 to 1.29%), a higher correct rate of cloudy pixels (CR > 80%), and a higher correct rate of clear-sky pixel (SR > 92%) rates compared with the real cloud account (CA). In addition, the UDTCD detected the edge of a broken cloud more accurately with a lower Error Rate (ER ~ 0.31–7.46%) and Missing Rate (MR < 20%) (Table 4).

Thick clouds exist in large patches with greater cloud content in the image and are easily identified. Unlike the blurred boundaries of thick clouds, thin clouds are not obvious and are identified with difficulty using traditional threshold methods. However, the UDTCD presents generally higher detection accuracy for both thick and thin clouds over vegetation and water areas (Figures 13e–13h). The evaluation results showed that the UDTCD cloud masks are more consistent and have lower CAE (~0.19 to 1.85%), higher CR (>92%), and higher SR (>91%) values than the real reference cloud mask. Moreover, the UDTCD can detect most thin clouds and the edges of thick clouds more accurately with lower ER and MR values of less than 9% and 8%, respectively (Table 4).

Bright areas refer to land use types (bare land, deserts with little vegetation cover, etc.) with higher surface reflectance and exhibit spectral characteristics similar to those of clouds, which are difficult to distinguish from clear sky. However, the UDTCD presents better overall cloud detection results over desert and bare land areas covered with broken, thick, and thin clouds (Figures 13i–13l). Evaluation results indicate that the UDTCD cloud mask has greater consistency with lower CAE (~0.60 to 2.74%), higher CR (>82%), and higher SR (>97%) values compared with the reference cloud mask. The UDTCD can better detect both thick and broken clouds and has good detection accuracy for thin clouds with a lower ER and MR of less than 3% and 18%, respectively (Table 4).

## 5.2. Evaluation and Comparison of the UDTCD Cloud Mask for MODIS

### 5.2.1. Evaluation of the UDTCD Cloud Mask

Figure 14 shows typical UDTCD cloud detection results for broken clouds (Figures 14a–14d) and thick and thin clouds (Figures 14e–14h) over different land use covers (Figures 14i–14l for bright areas) for MODIS data. Table 5 shows the corresponding evaluation of cloud detection results for the MODIS data shown in Figure 14. Evaluation results indicate that the UDTCD can identify most broken clouds irregularly distributed in the image (Figures 14a–14d) with higher CR (>91%) and higher SR (>94%) rates and overall lower CAE (<4%), ER (<6%), and MR (<9%) values compared with the reference cloud mask. The UDTCD has excellent detection accuracy for thick clouds and can also detect most thin clouds as well as the edges of thick clouds over different areas (Figures 14e–14h). The new algorithm shows overall higher CR (>80%) and SR (>96%) values and lower CAE (~0.25 to 3.26%), ER (<4%), and MR (<20%) values. For bright areas, the UDTCD can correctly differentiate thick clouds from clear sky and effectively detect broken and thin clouds (Figures 14i–14l) with overall higher CR (~73–93%) and SR (>92%) values and relatively lower CAE, ER, and MR values. Validation results show that the UDTCD has an overall higher cloud detection accuracy with higher SR (>92%) and lower CAE (~0.12 to 3.26%) values for broken, thick, and thin clouds over different land uses, particularly for bright areas.

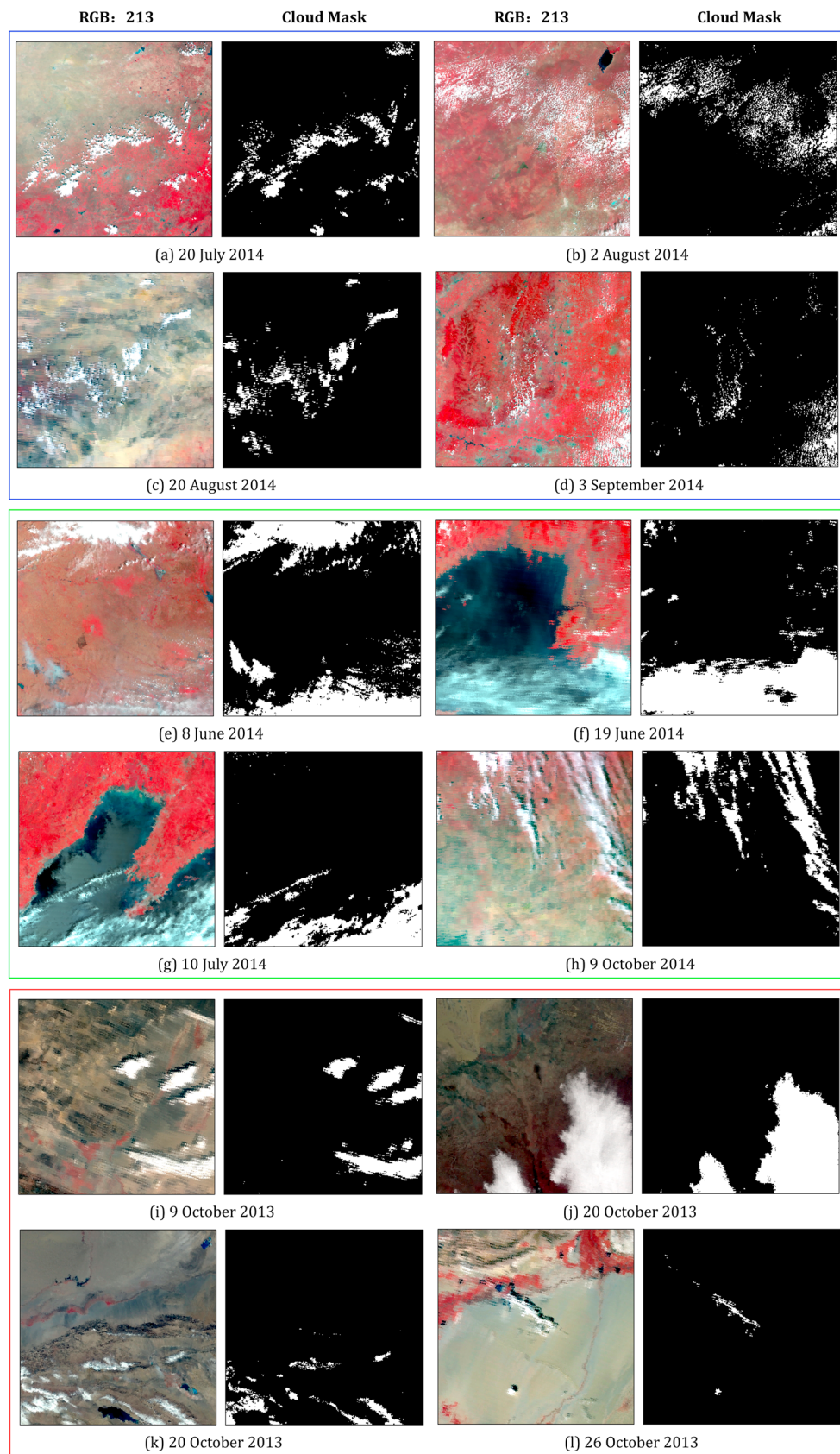


**Figure 14.** UDTCDa cloud detection results for different cloud types over different regions based on MODIS data.

**Table 5.** Evaluation of UDTCD Cloud Detection Results Based On MODIS Data

Cloud Types	No.	CA <sub>real</sub> (%)	CA <sub>new</sub> (%)	MAE (%)	CR (%)	ER (%)	MR (%)	SR (%)	Land cover
Broken cloud	a	4.71	5.13	+0.42	91.16	1.37	8.84	98.63	Vegetation
	b	7.63	10.31	+2.68	98.08	3.06	1.92	96.94	Vegetation
	c	25.76	28.88	+3.12	95.36	5.81	4.64	94.19	Bare land
	d	43.90	45.24	+1.34	95.65	5.79	4.35	94.21	Vegetation
Thick and Thin cloud	e	32.91	29.64	-3.26	84.85	2.57	15.15	97.43	Vegetation
	f	31.64	28.95	-2.69	86.83	2.16	13.17	97.84	Vegetation and Water
	g	17.08	17.33	+0.25	84.61	3.47	15.39	96.53	Water
	h	10.52	7.50	-3.02	80.21	0.97	19.79	99.04	Vegetation
Bright areas	i	8.27	8.33	+0.43	92.48	2.50	7.52	97.50	Bare land
	j	21.30	21.45	+0.15	80.22	7.84	19.78	92.16	Desert
	k	6.16	4.31	-1.85	76.85	0.40	23.15	99.60	Bare land and Desert
	l	0.68	0.55	-0.12	73.47	0.13	26.53	99.87	Desert

### 5.2.2. Compared With MODIS Cloud Mask Products

For comparison purposes, the MOD04 and MOD35 cloud mask products corresponding to the same time and area as the UDTCD cloud mask retrieved from MODIS images were obtained. Figures 15–17 compare the UDTCD and MODIS cloud mask products covered with different cloud types over different areas. The

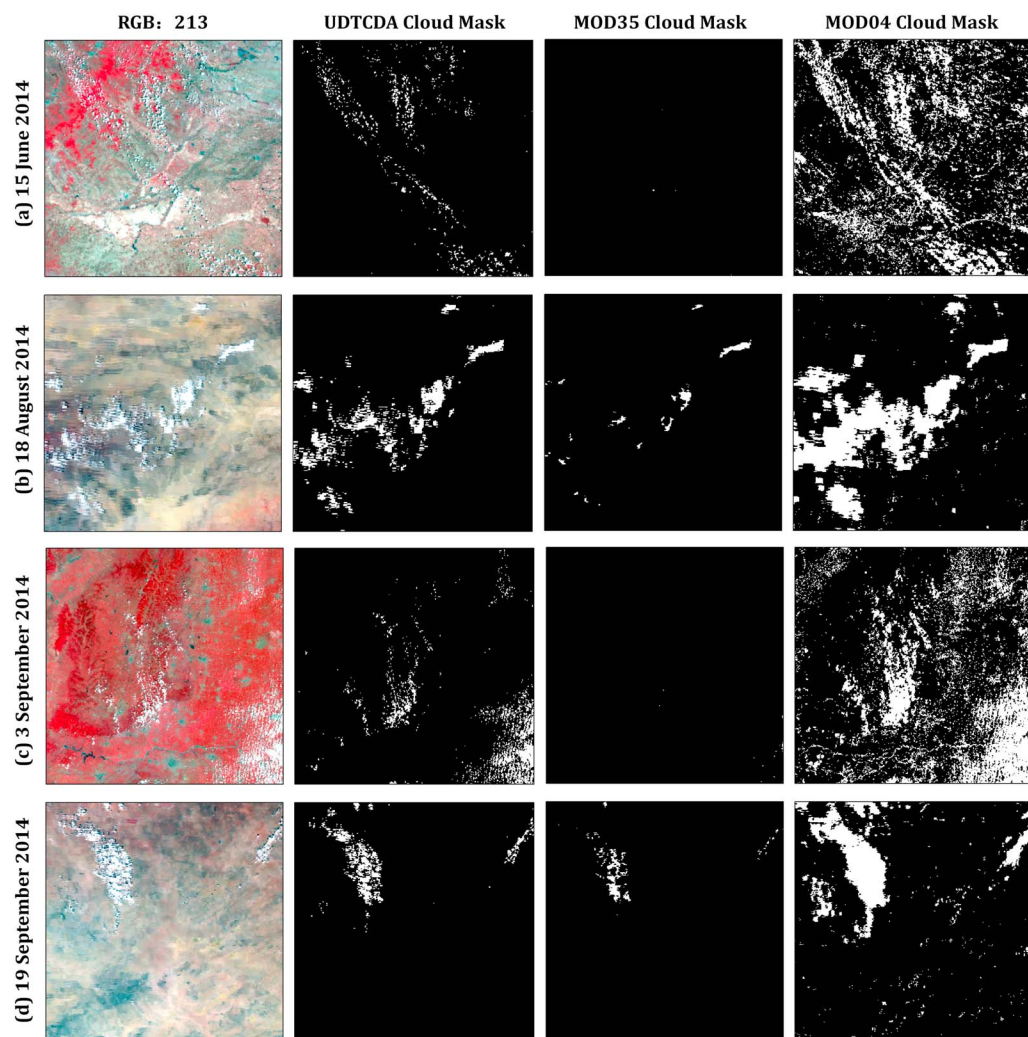


**Figure 15.** Comparison of broken cloud detection results between different cloud mask products.

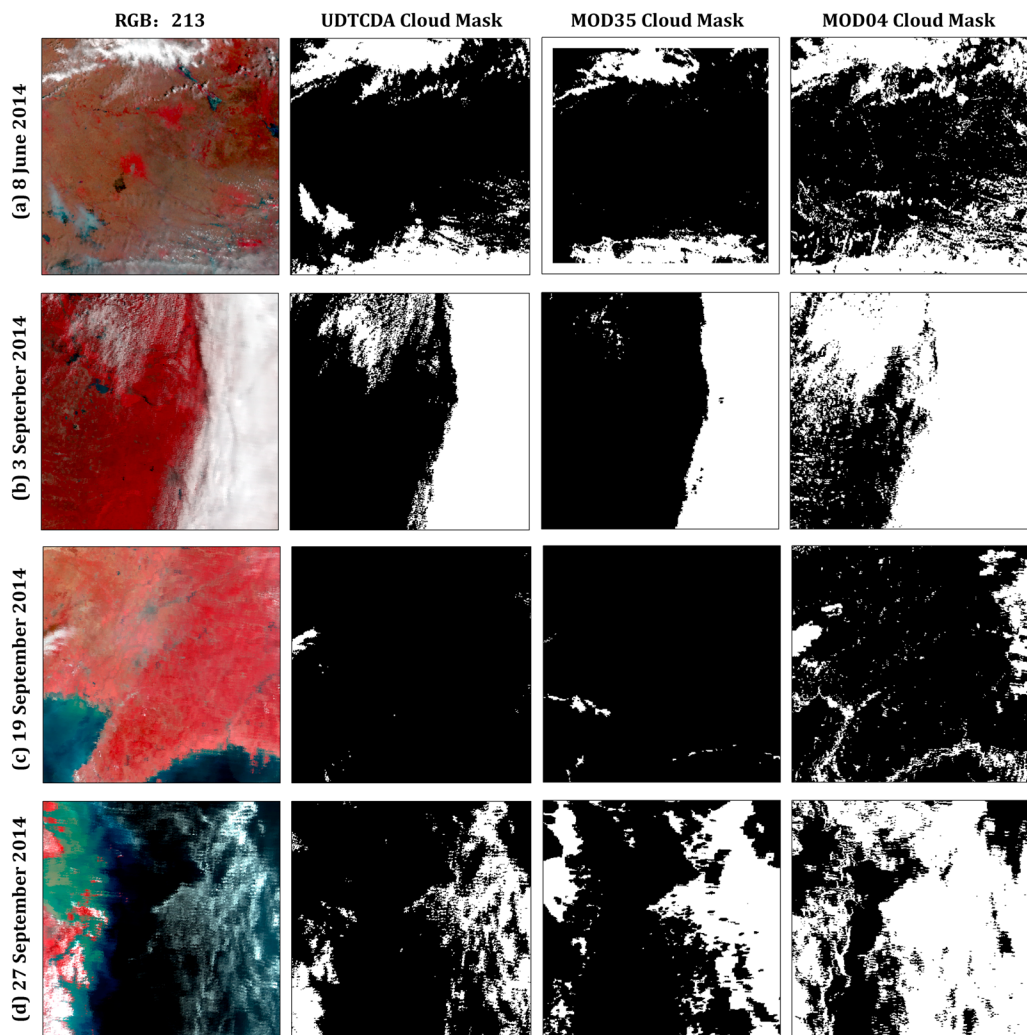


**Figure 16.** Comparison of thick and thin clouds detection results between different cloud mask products.

horizontal groups comprise the MODIS standard false-color composite images, the UDTIDA cloud mask, and MOD35 and MOD04 cloud masks. Table 6 compares their corresponding accuracy.

Figure 15 compares different cloud mask products for broken clouds. Evaluation results indicate that the MOD35 cloud mask showed overall lower cloud detection accuracy with a lower CR less than 30% and seriously underestimated the image cloud content ( $CAE \sim -0.76$  to 4.95%). However, the MOD04 cloud mask showed generally lower detection accuracy with lower SC values less than 53% and seriously overestimated the image cloud content ( $CAE \sim 1.64$  to 19.36%). In addition, the UDTIDA cloud mask showed better cloud detection results for broken clouds with higher CR and SR values greater than 82%; the UDTIDA cloud mask also had a lower uncertainty rate ( $CAE \sim -0.13$  to 0.11%) with smaller ER and MR values of less than 1.2% and 18%, respectively.

Figure 16 compares the cloud detection results of different cloud mask products for thick and thin clouds. Clearly, all cloud mask algorithms can better detect the thick clouds correctly in the images but show great differences in detection accuracy for thin clouds. Evaluation results indicate that the MOD35 cloud mask algorithm cannot identify most thin clouds and underestimates the image cloud content ( $CAE \sim -0.13$  to 18.63%), resulting in generally poorer detection accuracy with higher MR (~16.54 to 97.11%) and lower CR values of less than 83%. However, the MOD04 cloud mask algorithm seriously overestimated the cloud content of thin clouds in the image ( $CAE \sim 4.72$  to 35.96%), leading to an overall lower detection accuracy with a higher ER (~11.91 to 55.42%) and lower SC values of less than 53%. However, the UDTIDA showed better cloud

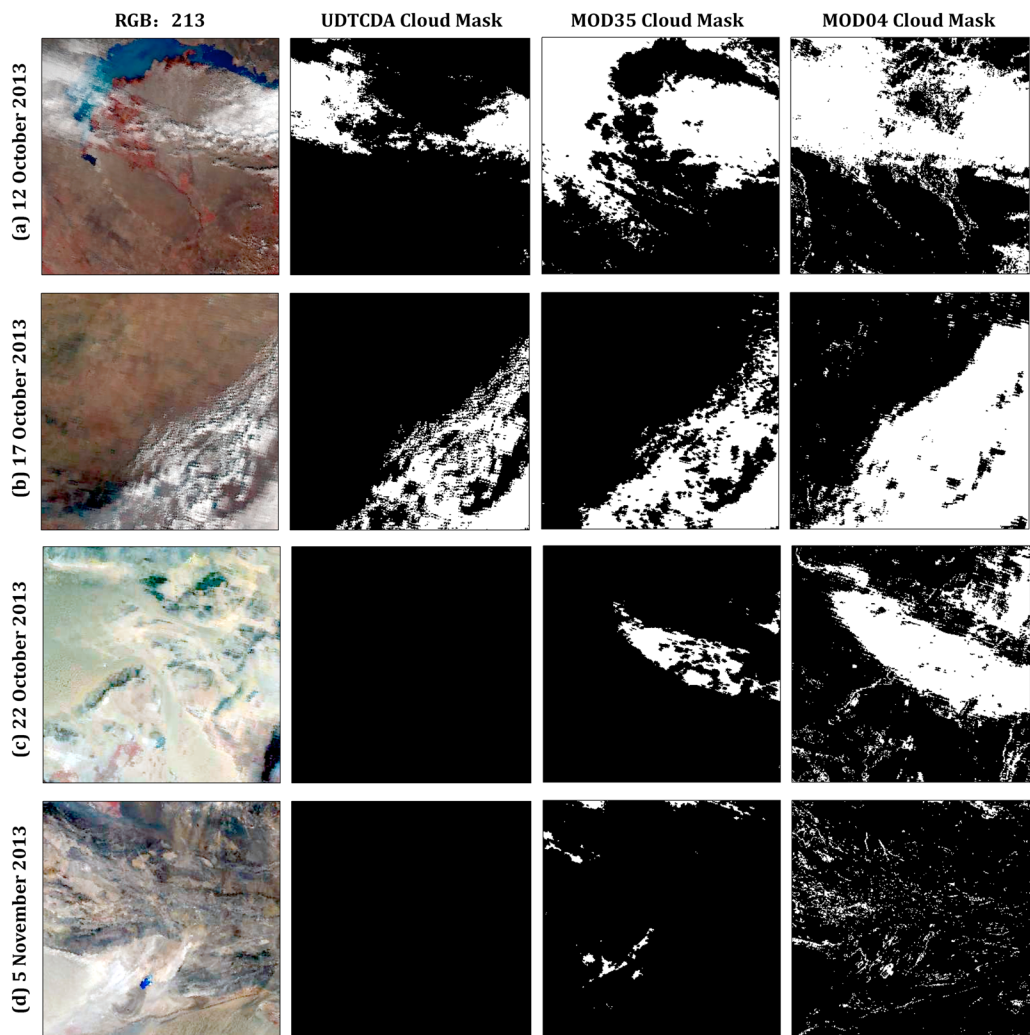


**Figure 17.** Comparison of cloud detection results between different cloud mask products over bright areas.

detection results for thick and thin clouds with higher CR and SR values greater than 82% and lower estimation errors (CAE  $\sim$  -3.26 to 0.34%) and ER and MR values of less than 5.79% and 17.6%, respectively.

Figure 17 compares different cloud mask products covered with different cloud types over bright areas. Both the UDTCDAs and MODIS cloud mask algorithms can detect most thick and thin clouds over bright areas more accurately but show poorer detection results for broken clouds and the edges of clouds. Evaluation results indicate that both MOD35 and MOD04 cloud masks seriously overestimated the image cloud content (CAE  $\sim$  3.05 to 28.79% for MOD35 and CAE  $\sim$  6.32 to 28.32% for MOD04 cloud mask) with higher ER values, leading to overall lower cloud detection accuracy. The estimation uncertainties are serious, particularly in bright areas with higher surface reflectance. Overall, however, the UDTCDAs shows better cloud detection accuracy for broken, thick, and thin clouds over bright areas with higher CR and SR values greater than 80% and lower CAE (0 to 1.5%) values, which can effectively reduce the estimation uncertainty in bright areas.

### 5.2.3. Comparison With the CALIPSO Cloud Product

The UDTCDAs cloud products were generated from the MODIS Aqua data from June to August in 2014 and were compared and validated with the CALIPSO cloud product. The selected data covered a large area, with a latitudinal range of 5 to 50°N and a longitudinal range of 75° to 135°E, and included different cloud types over different land surfaces. The corresponding MODIS Aqua MYD35 (C6) and MYD04 (C6) cloud mask products were also collected and compared to the CALIPSO cloud product. Four evaluation indexes, i.e., CR, SR, ER, and MR, were calculated, and the results are shown in Table 7.

**Table 6.** Evaluation and Comparison of Different Cloud Mask Products With Visual Interpretation of Clouds

Figure	CA <sub>real</sub> (%)	Algorithm	CA <sub>product</sub> (%)	MAE (%)	CR (%)	ER (%)	MR (%)	SR (%)
Figure 15a	1.96	UDTCDA	1.83	-0.13	82.22	0.22	17.78	99.78
		MOD35	0.01	-1.96	0.41	0.00	99.59	100.00
		MOD04	21.33	+19.36	47.24	20.81	52.76	79.19
Figure 15b	4.73	UDTCDA	4.74	+0.01	86.07	0.71	13.93	99.29
		MOD35	0.71	-4.02	13.56	0.07	86.44	99.93
		MOD04	15.34	+10.61	71.98	12.53	28.02	87.47
Figure 15c	5.16	UDTCDA	6.27	+1.11	99.58	1.19	0.42	98.81
		MOD35	0.21	-4.95	4.06	0.00	95.94	100.00
		MOD04	6.80	+1.64	88.63	21.97	11.37	78.03
Figure 15d	1.55	UDTCDA	2.39	-0.84	98.17	0.88	1.83	99.12
		MOD35	0.79	-0.76	30.25	0.32	69.75	99.68
		MOD04	10.10	+8.55	94.88	8.74	5.12	91.26
Figure 16a	32.91	UDTCDA	29.64	-3.26	84.85	2.57	15.15	97.43
		MOD35	14.28	-18.63	43.09	0.16	56.91	99.84
		MOD04	37.83	+4.92	81.30	16.50	18.70	83.50
Figure 16b	43.90	UDTCDA	45.24	+1.34	95.65	5.79	4.35	94.21
		MOD35	36.86	-7.04	83.46	0.39	16.54	99.61
		MOD04	71.53	+27.63	99.24	49.85	0.76	50.15
Figure 16c	1.71	UDTCDA	1.10	+0.62	84.69	0.10	15.31	99.90
		MOD35	0.58	-1.13	2.89	0.55	97.11	99.45
		MOD04	12.77	+11.06	80.77	11.91	19.23	88.09
Figure 16d	24.32	UDTCDA	21.74	+2.58	82.40	2.24	17.60	97.76
		MOD35	32.00	+7.68	70.40	19.66	29.60	80.34
		MOD04	61.88	+37.56	81.98	55.42	18.02	44.58
Figure 17a	14.94	UDTCDA	16.44	+1.50	89.69	4.70	10.31	95.30
		MOD35	43.74	+28.79	96.99	35.20	3.01	64.80
		MOD04	43.38	+28.44	98.74	34.51	1.26	65.49
Figure 17b	21.30	UDTCDA	21.45	+0.15	80.22	7.84	19.78	92.16
		MOD35	25.20	+3.90	75.98	13.44	24.02	86.56
		MOD04	44.85	+23.55	91.98	33.93	8.02	66.07
Figure 17c	0.00	UDTCDA	0.00	0.00	100.00	0.00	0.00	100.00
		MOD35	3.05	+3.05	0.00	3.05	100.00	96.95
		MOD04	6.32	+6.32	0.00	6.32	100.00	93.68
Figure 17d	0.00	UDTCDA	0.00	0.00	100.00	0.00	0.00	100.00
		MOD35	6.04	+6.04	0.00	6.04	100.00	93.96
		MOD04	28.32	+28.32	0.00	28.32	100.00	71.68

Table 7 shows that the MOD35 cloud products have an overall lower consistency with the CALIPSO cloud products, with an average SR value of 61% and a higher MR value of 34.53%. The higher CR (75.36%) and relatively smaller ER (19.98%) indicate that the MOD35 cloud products seriously underestimated the cloud information in the images. The MOD04 cloud products showed an overall higher SR (92%), a smaller MR

**Table 7.** Evaluation and Comparison of Different MODIS Cloud Products to the CALIPSO Cloud Product

	UDTCDA Cloud Product				MYD35 Cloud Product				MYD04 Cloud Product			
	CR (%)	ER (%)	MR (%)	SR (%)	CR (%)	ER (%)	MR (%)	SR (%)	CR (%)	ER (%)	MR (%)	SR (%)
12 June	90.42	22.24	9(58	77.76	77.05	0.00	14.00	79.97	97.40	50.07	2.60	49.93
17 June	82.84	15.71	17.16	84.29	41.52	1.83	43.53	95.81	96.40	85.74	3.60	14.26
23 June	83.28	12.50	16.72	87.50	72.32	21.58	26.96	72.98	96.40	85.74	3.60	14.26
5 July	81.28	13.08	18.72	86.92	66.43	23.84	33.57	76.16	93.28	61.69	6.72	38.31
10 July	83.68	10.00	16.32	90.00	60.42	68.31	39.58	31.69	83.91	62.94	16.09	37.06
16 July	81.68	19.44	18.32	80.56	60.58	0.53	32.90	79.68	81.93	57.99	18.07	42.01
26 July	78.90	28.80	21.10	71.20	35.81	16.08	46.20	80.23	89.08	61.53	10.92	38.47
7 August	78.14	18.97	21.86	81.03	64.38	17.51	35.62	82.49	92.53	67.15	7.47	32.85
12 August	72.80	22.48	27.20	77.52	59.22	20.68	40.78	79.32	89.11	67.66	10.89	32.34
20 August	81.65	28.28	18.35	71.72	65.07	15.62	34.94	84.38	95.78	88.53	4.22	11.47
25 August	75.75	27.01	24.25	72.99	68.23	33.76	31.77	66.24	96.22	80.13	3.78	19.87
Average	80.95	19.86	19.05	80.14	61.00	19.98	34.53	75.36	92.00	69.92	8.00	30.08

(8%), an average CR of less than 40%, and a higher average ER of 69.92%, indicating that it seriously overestimated the cloud information in the images. Compared with the MOD35 and MOD04 cloud products, the UDTCDAs cloud products showed a better consistency with CALIPSO cloud products with CR and SR values greater than 80% and ER and MR values less than 20%. The UDTCDAs can identify clouds more accurately, thereby effectively reducing the estimation uncertainty compared with the current MODIS cloud products.

## 6. Conclusions

To reduce the influence of mixed pixels formed of cloud and ground features on cloud detection and improve the cloud identification ability of land satellites with high spatial resolutions but low spectral resolutions, a new Universal Dynamic Threshold Cloud Detection Algorithm (UDTCDA) with a surface reflectance database support is proposed in this paper. A monthly surface reflectance database was established based on the long-time series of MODIS 8 day synthetic surface reflectance products (MOD09A1). The relation between the apparent reflectance and the surface reflectance was simulated using the 6S model, carefully considering different observation and atmospheric conditions. Then, the dynamic cloud detection models were built and applied to two typical sets of selected data—MODIS and Landsat 8—to perform cloud detection experiments. A visual interpretation of the clouds and the CALIPSO Lidar cloud estimates were selected to verify the experimental results, and the results were also compared with the current MODIS cloud products.

The evaluation and comparison results indicate that the MOD35 cloud products exhibited an overall low cloud detection accuracy, with a low correct rate of cloudy pixels (CR) of less than 30%. These products seriously underestimated the cloud content in the images. Similarly, the MOD04 cloud products had an overall lower detection accuracy with a lower correct rate of clear-sky pixels (SR) less than 60% and seriously overestimated the cloud content in the images. The UDTCDAs cloud products were considerably more consistent with the visual interpretation and CALIPSO-derived cloud estimates and demonstrated overall better cloud detection accuracy, with higher SR and CR values of greater than 80% and lower Error Rate (ER) and Missing Rate (MR) values of less than 20%. Therefore, the UDTCDAs products exhibit less uncertainty than the MOD04 and MOD35 cloud mask products. The UDTCDAs can effectively reduce the effects of mixed pixels and atmospheric factors and can achieve cloud detection from a large-scale area and long-term sequence for different satellite data. These capabilities make the products highly valuable for retrieval of atmospheric and surface parameters.

This study found that the new algorithm shows better and more effective cloud detection results. However, some problems still remain.

1. The UDTCDAs with the prior monthly surface reflectance database support is established based on the assumption that the surface reflectance of most features changes little within a certain period. Thus, this algorithm can be limited in some areas where the surface reflectance changes obviously due to snowfall/melt, forest fires, logging, urban expansion, etc.
  2. The cloud detection accuracy may decrease due to the lack of terrain correction in the MODIS surface reflectance products over areas of rugged terrain.
  3. Due to the lack of ground measurements of clouds, the validation work was performed via comparisons with the remote sensing visual interpretations of clouds, which is a more subjective approach.
- Thus, more comprehensive and effective verification work needs to be performed in future studies.

## References

- Ackerman, S., R. Frey, K. Strabala, Y. Liu, L. Gumley, B. Baum, and P. Menzel (2010), Discriminating clear-sky from cloud with modis algorithm – theoretical basis document (MOD35), 117 pp., Modis Cloud Mask Team Coop. Inst. for Meteorol. Satell. Stud.
- Baldridge, A. M., S. J. Hook, C. I. Grove, and G. Rivera (2009), The ASTER spectral library version 2.0, *Remote Sens. Environ.*, 113, 711–715, doi:10.1016/j.rse.2008.11.007.
- Chepfer, H., S. Bony, D. Winker, G. Cesana, J. L. Dufresne, P. Minnis, C. J. Stubenrauch, and S. Zeng (2010), The GCM-oriented CALIPSO cloud product (CALIPSO-GOCCP), *J. Geophys. Res.*, 115, D00H16, doi:10.1029/2009JD012251.
- Clark, C., and J. Boyce (1999), The detection of ship trail clouds by artificial neural network, *Int. J. Remote Sens.*, 20, 711–726, doi:10.1080/014311699213154.
- Cukier, R. I., C. M. Fortuin, K. E. Shuler, A. G. Petschek, and J. H. Schaibly (1973), Study of the sensitivity of coupled reaction systems to uncertainties in rate coefficients. I Theory, *J. Chem. Phys.*, 59, 3873–3878, doi:10.1063/1.1680571.

## Acknowledgments

The MODIS products are available at the Goddard Space Flight Center (GSFC) Level 1 and Atmosphere Archive and Distribution System (<http://ladsweb.nascom.nasa.gov/>); the Landsat 8 OLI data are available from the Earth Resources Observation and Science Center (EROS) (<http://glovis.usgs.gov/>); and the CALIPSO products are available from the Earth Observing System Data and Information System Earth (EOSDIS) (<https://earthdata.nasa.gov/>). The authors thank the National Natural Science Foundation of China (41171270), the Outstanding Youth Foundation of Shandong Province (JQ201211) and the Graduate Innovation Foundation of Shandong University of Science and Technology (YC150103). The authors declare no conflict of interest.

- Fisher, A. (2014), Cloud and cloud-shadow detection in SPOT5 HRG imagery with automated morphological feature extraction, *Remote Sens.*, 6, 776–800, doi:10.3390/rs6010776.
- Gao, B. C., P. Yang, and R. R. Li (2003), Detection of high clouds in polar regions during the daytime using the MODIS 1.375- $\mu$ m channel, *IEEE Trans. Geosci. Remote Sens.*, 41, 474–481, doi:10.1109/TGRS.2002.808290.
- Greenhough, J., J. J. Remedios, H. Sembhi, and L. J. Kramer (2005), Towards cloud detection and cloud frequency distributions from MIPAS infra-red observations, *Adv. Space Res.*, 36, 800–806, doi:10.1016/j.asr.2005.04.096.
- Hagolle, O., M. Huc, D. V. Pascual, and G. Dedieu (2010), A multi-temporal method for cloud detection, applied to FORMOSAT-2, VEN mu S, LANDSAT and SENTINEL-2 images, *Remote Sens. Environ.*, 114, 1747–1755, doi:10.1016/j.rse.2010.03.002.
- Hai, Q. S., Y. H. Bao, B. A. O. Alatengtuoya, and L. B. Guo (2009), New method to identify sand and dust storm by using remote sensing technique—With Inner Mongolia autonomous region as example, *J. Infrared Millimeter Waves*, 2, 129–132.
- Hall, D. K., G. A. Riggs, and V. V. Salomonson (1995), Development of methods for mapping global snow cover using moderate resolution imaging spectroradiometer data, *Remote Sens. Environ.*, 54, 127–140, doi:10.1016/0034-4257(95)00137-P.
- Hall, D. K., G. A. Riggs, V. V. Salomonson, N. E. DiGirolamo, and K. J. Bayr (2002), MODIS snow-cover products, *Remote Sens. Environ.*, 83, 181–194, doi:10.1016/S0034-4257(02)00095-0.
- Hu, Y. (2007), Depolarization ratio-effective Lidar ratio relation: Theoretical basis for space Lidar cloud phase discrimination, *Geophys. Res. Lett.*, 34, L11812, doi:10.1029/2007GL029584.
- Hu, Y., et al. (2009), CALIPSO/CALIOP cloud phase discrimination algorithm, *J. Atmos. Oceanic Technol.*, 26, 2293–2309, doi:10.1175/2009JTECHA1280.1.
- Hutchinson, K. D., and K. R. Hardy (1995), Threshold functions for automated cloud analyses of global meteorological satellite imagery, *Int. J. Remote Sens.*, 16, 3665–3680, doi:10.1080/01431169508954653.
- Jedlovec, G. J., S. L. Haines, and F. J. LaFontaine (2008), Spatial and temporal varying thresholds for cloud detection in GOES imagery, *IEEE Trans. Geosci. Remote Sens.*, 46, 1705–1717, doi:10.1109/TGRS.2008.916208.
- Karlsson, K. (1989), Development of an operational cloud classification model, *Int. J. Remote Sens.*, 10, 687–693, doi:10.1080/01431168908903910.
- Kärner, O. (2000), A multi-dimensional histogram technique for cloud classification, *Int. J. Remote Sens.*, 21, 2463–2478, doi:10.1080/01431160050030565.
- Kazantzidis, A., K. Eleftheratos, and C. S. Zerefos (2011), Effects of cirrus cloudiness on solar irradiance in four spectral bands, *Atmos. Res.*, 102, 452–459, doi:10.1016/j.atmosres.2011.09.015.
- Kazantzidis, A., P. Tzoumanikas, A. F. Bais, S. Fotopoulos, and G. Economou (2013), Cloud detection and classification with the use of whole-sky ground-based images, in *Advances in Meteorology, Climatology and Atmospheric Physics*, pp. 80–88, Springer, Berlin.
- Keshava, N., and J. F. Mustard (2002), Spectral unmixing, *IEEE Signal Process. Mag.*, 19, 44–57, doi:10.1109/79.974727.
- Klein, A., and A. C. Barnett (2003), Validation of daily MODIS snow cover maps of the Upper Rio Grande River Basin for the 2000–2001 snow year, *Remote Sens. Environ.*, 86, 162–176, doi:10.1016/S0034-4257(03)00097-X.
- Kotchenova, S. Y., E. F. Vermote, R. Matarrese, and K. F. Jr. (2006), Validation of a vector version of the 6s radiative transfer code for atmospheric correction of satellite data, part i: Path radiance, *Appl. Opt.*, 45(26), 6762–6774.
- Kriebel, K. T., G. Gesell, M. Kästner, and H. Mannstein (2003), The cloud analysis tool APOLLO: Improvements and validations, *Int. J. Remote Sens.*, 24, 2389–2408, doi:10.1080/01431160210163065.
- Levy, R. C., S. Mattoe, L. A. Munchak, L. A. Remer, A. M. Sayer, and N. C. Hsu (2013), The collection 6 MODIS aerosol products over land and ocean, *Atmos. Meas. Tech. Discuss.*, 6, 159–259, doi:10.5194/amt-6-159-2013.
- Li, Q., W. Lu, and J. Yang (2011), A hybrid thresholding algorithm for cloud detection on ground-based color images, *J. Atmos. Oceanic Technol.*, 28, 1286–1296, doi:10.1175/JTECH-D-11-00009.1.
- Lin, J., X. Feng, P. Xiao, H. Li, J. Wang, and Y. Li (2012), Comparison of snow indexes in estimating snow cover fraction in a mountainous area in northwestern China, *IEEE Geosci. Remote Sens. Lett.*, 9, 725–729, doi:10.1109/LGRS.2011.2179634.
- Liu, C. L., and B. F. Wu (2004), Application of cloud detection algorithm for the AVHRR data, *J. Remote Sens.*, 8, 677–687.
- Miao, Z., R. G. Lathrop, M. Xu, I. P. La Puma, K. L. Clark, J. Hom, N. Skowronski, and S. van Tuyl (2011), Simulation and sensitivity analysis of carbon storage and fluxes in the New Jersey Pinelands, *Environ. Model. Software*, 26, 1112–1122, doi:10.1016/j.envsoft.2011.03.004.
- Molnar, G., and J. A. Coakley (1985), Retrieval of cloud cover from satellite imagery data: A statistical approach, *J. Geophys. Res.*, 90, 12,960–12,970, doi:10.1029/JD090iD07p12960.
- Nakajima, T. Y., T. Tsuchiya, H. Ishida, T. N. Matsui, and H. Shimoda (2011), Cloud detection performance of space borne visible-to-infrared multispectral imagers, *Appl. Opt.*, 50, 2601–2616, doi:10.1364/AO.50.002601.
- Pandya, N., N. Gabas, and E. Marsden (2012), Sensitivity analysis of Phast's atmospheric dispersion model for three toxic materials (nitric oxide, ammonia, chlorine), *J. Loss Prev. Process Ind.*, 25, 20–32, doi:10.1016/j.jlp.2011.06.015.
- Poole, L. R., D. M. Winker, J. R. Pelon, and M. P. McCormick (2002), Calipso: Global aerosol and cloud observations from lidar and passive instruments, Proc. SPIE 4881, Sensors, Systems, and Next-Generation Satellites VI, 419 (April 8, 2003), Crete, Greece, doi:10.1117/12.462519.
- Powell, K. A. (2005), The development of the CALIPSO lidar simulator, Optical Radar.
- Powell, K. A., et al. (2009), CALIPSO Lidar calibration algorithms. Part I: Nighttime 532-nm parallel channel and 532-nm perpendicular channel, *J. Atmos. Oceanic Technol.*, 26, 2015–2033, doi:10.1175/2009JTECHA1242.1.
- Powell, K. A., M. Vaughan, D. Winker, K. P. Lee, M. Piyy, and C. Trepte (2013), Cloud-aerosol LIDAR infrared pathfinder satellite observations data management system, data products catalog, Document No: PC-SCI-503, Release 3.6, Sept. 3.
- Remer, L. A., D. Tanre, Y. J. Kaufman, R. C. Levy, and S. Mattoe (2006), Algorithm for remote sensing of tropospheric aerosol from MODIS: Collection 005. Algorithm theoretical basis. [Available at <http://lmodisatmos.gsfc.nasa.gov/reference-atbd.php>.]
- Remer, L. A., S. Mattoe, R. C. Levy, A. Heidinger, R. B. Pierce, and M. Chin (2012), Retrieving aerosol in a cloudy environment: Aerosol product availability as a function of spatial resolution, *Atmos. Meas. Tech.*, 5, 1823–1840, doi:10.5194/amt-5-1823-2012.
- Rosswall, W. B., and L. C. Garder (1993), Cloud detection using satellite measurements of infrared and visible radiances for ISCCP, *J. Clim.*, 6, 2341–2369, doi:10.1175/1520-0442(1993)006<2341:CDUSMO>2.0.CO;2.
- Rosswall, W. B., and R. A. Schiffer (1991), Cloud data products, *Bull. Am. Meteorol. Soc.*, 27, 2–20.
- Salomonson, V. V., and I. Appel (2006), Development of the Aqua MODIS NDSI fractional snow cover algorithm and validation results, *IEEE Trans. Geosci. Remote Sens.*, 44(7), 1747–1756, doi:10.1109/TGRS.2006.876029.
- Saltelli, A., S. Tarantola, and K. P. S. Chan (1999), A quantitative model-independent method for global sensitivity analysis of model output, *Technometrics*, 41, 39–56, doi:10.1080/00401706.1999.10485594.
- Saltelli, A., P. Annoni, I. Azzini, F. Campolongo, M. Ratto, and S. Tarantola (2010), Variance based sensitivity analysis of model output. Design and estimator for the total sensitivity index, *Comput. Phys. Commun.*, 181, 259–270.
- Sassen, K., Z. Wang, and D. Liu (2008), Global distribution of cirrus clouds from CloudSat/Cloud-Aerosol Lidar and infrared Pathfinder satellite observations (CALIPSO) measurements, *J. Geophys. Res.*, 113, D00A12, doi:10.1029/2008JD009972.

- Saunders, R. W., and K. T. Kriebel (1988), An improved method for detecting clear sky and cloudy radiances from AVHRR data, *Int. J. Remote Sens.*, 9, 123–150, doi:10.1080/01431168808954841.
- Sèze, G., and W. B. Rossow (1991), Time-cumulated visible and infrared radiance histograms used as descriptors of surface and cloud variations, *Int. J. Remote Sens.*, 12, 877–920, doi:10.1080/01431169108929702.
- Stowe, L. L., E. P. McClain, R. Carey, P. Pellegrino, G. G. Gutman, P. Davis, C. Long, and S. Hart (1991), Global distribution of cloud cover derived from NOAA/AVHRR operational satellite data, *Adv. Space Res.*, 11, 51–54, doi:10.1016/0273-1177(91)90402-6.
- Sun, L., J. Wei, M. Bilal, X. Tian, C. Jia, Y. Guo, and X. Mi (2016), Aerosol optical depth retrieval over bright areas using landsat 8 OLI images, *Remote Sens.*, 8, 23, doi:10.3390/rs8010023.
- Turner, J., G. J. Marshall, and R. S. Ladkin (2001), An operational, real-time cloud detection scheme for use in the Antarctic based on AVHRR data, *Int. J. Remote Sens.*, 22, 3027–3046, doi:10.1080/01431160121291.
- Varella, H., M. Guérif, and S. Buis (2010), Global sensitivity analysis measures the quality of parameter estimation: The case of soil parameters and a crop model, *Environ. Modell. Software*, 25, 310–319, doi:10.1016/j.envsoft.2009.09.012.
- Vermote, E. F., and S. Y. Kotchenova (2008), MOD09 user's Guide [J/OL]. [Available at <http://modis-sr.ltdri.org/>.]
- Vermote, E. F., and A. Vermeulen (1999), ATBD: Atmospheric correction algorithm: Spectral reflectances (MOD09) Version 4.0, NASA contract NAS5-96062.
- Vermote, E. F., D. Tanré, J. L. Deuzé, M. Herman, and J. J. Morcette (1997), Second simulation of the satellite signal in the solar spectrum, 6 s: An overview, *IEEE Trans. Geosci. Remote Sens.*, 35, 675–686, doi:10.1109/36.581987.
- Walder, P., and I. McLaren (2000), Neural network based methods for cloud classification on AVHRR images, *Int. J. Remote Sens.*, 21, 1693–1708, doi:10.1080/014311600209977.
- Wei, J., Y. F. Ming, L. S. Han, Z. L. Ren, and Y. M. Guo (2015), [Method of remote sensing identification for mineral types based on multiple spectral characteristic parameters matching], *Guang Pu Xue Yu Guang Pu Fen Xi*, 35, 2862–2866.
- Winker, D. M., R. P. Jacques, and P. M. McCormick (2010), The CALIPSO mission: Spaceborne lidar for observation of aerosols and clouds, *Bull. Am. Meteorol. Soc.*, 91, 1211–1229.
- Wylie, D. P., and W. P. Menzel (1989), Two years of cloud cover statistics using VAS, *J. Clim. Appl. Meteorol.*, 2, 380–392.
- Wylie, D. P., W. P. Menzel, H. M. Woolf, and K. I. Strabala (1994), Four years of global cirrus cloud statistics using HIRS, *J. Clim.*, 7, 1972–1980.
- Zhang, Y., B. Guindon, and X. Li (2014), A robust approach for object-based detection and radiometric characterization of cloud shadow using haze optimized transformation, *IEEE Trans. Geosci. Remote Sens.*, 52, 5540–5547, doi:10.1109/TGRS.2013.2290237.
- Zhu, Z., and C. E. Woodcock (2012), Object-based cloud and cloud shadow detection in landsat imagery, *Remote Sens. Environ.*, 118, 83–94, doi:10.1016/j.rse.2011.10.028.
- Zhu, Z., S. Wang, and C. E. Woodcock (2015), Improvement and expansion of the Fmask algorithm: Cloud, cloud shadow, and snow detection for Landsats 4–7, 8, and Sentinel 2 images, *Remote Sens. Environ.*, 159, 269–277, doi:10.1016/j.rse.2014.12.014.